

A quantitative microscale dynamic column  
breakthrough apparatus for measurement of  
unary and binary adsorption equilibrium on  
milligram quantities of adsorbent

Nicholas Stiles Wilkins, James A. Sawada\*  
and Arvind Rajendran \*

Department of Chemical and Materials Engineering, University of Alberta

Donadeo Innovation Centre of Engineering, 9211-116 Street NW

Edmonton, Alberta, Canada T6G 1H9

January 8, 2022

## Abstract

A microscale dynamic column breakthrough ( $\mu$ DCB) apparatus with the ability to measure unary and binary adsorption equilibrium on a milligram-scale quantity of adsorbent is described. The  $\mu$ DCB is a low cost system that can be constructed through minor modifications of a commercial gas chromatograph and uses a thermal conductivity detector. The small scale of the apparatus allows for the rapid collection of dynamic column breakthrough experiments. The mass balances for adsorption and desorption experiments were derived along with a description of the blank. The  $\mu$ DCB apparatus was tested with 238.9 mg of zeolite 13X and 180.2 mg of activated carbon with single-component  $\text{N}_2/\text{He}$  and  $\text{CH}_4/\text{He}$  adsorption and desorption measurements. The measured equilibrium data agreed well with volumetrically collected data. These measurements are both accurate and precise. Multicomponent adsorption was also studied on zeolite 13X and activated carbon for  $\text{CH}_4/\text{N}_2$  and  $\text{CO}_2/\text{CH}_4$  mixtures. This data was compared with ideal and adsorbed solution theory, extended dual-site Langmuir calculations and the literature.

Keywords: dynamic column breakthrough, adsorption, equilibrium, multicomponent, competition, experimental protocol, data analysis

---

\*Author to whom correspondence should be addressed. Phone: +1.780.492.3912, E-mail: arvind.rajendran@ualberta.ca, sawada@ualberta.ca

# 1 Introduction

The design and optimization of separation processes rely on the availability of reliable thermodynamic and kinetic parameters. Several adsorption separations exploit the differences in equilibrium between the various species in the mixture [1–3]. At high concentrations adsorbing species compete (or in some cases co-operate) with each other for the available sites on the adsorbent. In some cases, the extent of this competition can be estimated, based on single component isotherms assuming ideality of the adsorbed phase [4]. However, there are several instances where this assumption does not hold good and experimental measurements are imperative [5–7]. Moreover, the use of incorrect competitive equilibria can have a impact on the prediction of process performances [8]. Databases of experimental multicomponent data do exist, but the data is limited [5, 9]. Also, as new adsorbents, e.g., metal-organic and covalent-organic frameworks are reported in the literature, multicomponent equilibrium data will need to be collected to ensure accurate process simulation on these materials. Note that these measurements can also be valuable for validating/comparing results from molecular simulations.

Several experimental techniques have been described in the literature for the measurement of multi-component adsorption equilibria [10]. A few examples include, Dynamic column breakthrough (DCB) [8, 11–14], volumetry+ gas chromatography (GC) [15, 16], volumetry+gravimetry [17], volumetry+GC [17, 18], concentration pulse chromatography [19, 20], zero-length column (ZLC) [21, 22], and the integral mass balance (IMB) method [23]. Multicomponent volumetry is performed by expanding a known quantity of multicomponent gas into a recirculating chamber with some adsorbent, and sampling the equilibrium gas composition with a GC [15, 16]. A recent multicomponent volumetry study by Shade *et al.* reported using a sample mass of  $\approx 5$  grams [16]. In the gravimetry+GC method, a mass of adsorbent is placed on a microbalance in a recirculating chamber, and is charged with an initial volume of known multicomponent gas [6, 17]. At equilibrium, the microbalance reading is used to deter-

mine the total loading, and the gas composition is measured by a gas chromatograph to solve for each component loading. Multicomponent gravimetry requires  $\approx 2 - 5$  grams of adsorbent that is measured on the microbalance, often with a secondary packed bed of adsorbent (in the circulating volume) containing tens of grams. This secondary packed bed inside the circulating volume is to change the fluid composition enough to determine the equilibrium mass balances reliably [18, 24]. Studies by Ottiger *et al.* used 2.97 g of adsorbent for the microbalance and 37.84 g for the secondary packed bed [18, 24]. The concentration pulse chromatography method introduces a small injection of an adsorbate mixture to a packed bed of interest to measure equilibrium. Data is collected dynamically to calculate equilibrium through a transient material balance. A study by Kennedy and Tezel used approximately 7 grams of adsorbent to measure binary equilibrium [20]. The ZLC technique measures multicomponent equilibrium by initially loading a mixture adsorbate onto a small quantity of adsorbent, and then sweeping that adsorbent with an inert gas [25]. The dynamic response is used to solve a transient material balance to calculate equilibrium [21, 22, 25]. ZLC uses a very small quantity of adsorbent, generally on the order of 5 – 10 milligrams [25]. The IMB method combines a DCB experiment with a gravimetric measurement, within the same instrument, to determine the component and total loadings [23]. In the study that introduced the method by Broom *et al.*, a sample size of 3.5 grams was utilized.

Dynamic column breakthrough is a useful technique to obtain adsorption equilibrium and kinetic data, as well as column dynamics for single or multi-component systems [12]. This technique considers a column packed with an adsorbent where a step function of an inert or adsorbing gas is introduced to the column in order to measure the composition and flow at the column outlet. By performing a mass balance, the adsorbed amount can be calculated. The advantage of the DCB method is that, as long as the composition of the outlet can be measured, the same experimental set-up can be used to measure both single, and multi-component equilibria. Dynamic column breakthrough experiments have classically been performed using fairly large quantities of pelletized or granulated adsorbent ( $> 10$  g of adsorbent). One benefit

of a large column breakthrough apparatus is that the blank response becomes more negligible compared to that from the column. Further, the DCB method is often seen as a technique that can be used to check the scalability of the adsorbent synthesis. For the characterization of new materials that are typically synthesized in small quantities, typically on the order of hundreds of milligrams to grams, the DCB method is often used only in a qualitative manner to demonstrate the separation capability and rarely as a quantitative tool.

The aim of this study is to build a micro-scale dynamic column breakthrough apparatus ( $\mu$ DCB) that can quantify single and multi-component adsorption equilibrium and column dynamics on a milligram-scale sized samples. This sample size represents the crystalline, as-synthesized, rare and difficult to scale-up materials. The  $\mu$ DCB was also constructed with the aim of keeping the overall costs low in order to facilitate its routine use in synthesis laboratories. We limited ourselves to only use components that are typically available in a material synthesis laboratory, e.g. GC, standard lab-scale flow controllers, flow meters and off-the shelf piping. The details of  $\mu$ DCB system and its operation are described. The system was tested with a series of  $N_2$  and  $CH_4$  single-component adsorption and desorption experiments and multi-component  $CH_4/N_2$  and  $CO_2/CH_4$  experiments on zeolite 13X and activated carbon.

## 2 Materials and Methods

The zeolite 13X (Zeochem Z10-02ND) sample used in this study is identical to the one in our previous studies. This was deliberately chosen in order to obtain consistent sets of equilibrium data [8,11]. A more detailed description of the zeolite 13X sample can be found in a previous publication [8]. The activated carbon used in this study (Calgon BPL 4x10 CAS#7440-44-00) is a widely studied commercial adsorbent [16, 26–29]. Both the zeolite 13X and activated carbon samples were originally pelleted. For this study, both were crushed and sieved to 16 – 18 mesh to pack into the 1/4" Swagelok VCR fittings. All gases in this study (99.99%  $CH_4$ , 99.998%  $CO_2$ , 99.999%  $N_2$  and

99.999% He) were obtained from Linde Canada.

## 2.1 Volumetric Experiments

Low-pressure volumetric equilibrium data for N<sub>2</sub>, CH<sub>4</sub> and CO<sub>2</sub> were measured with a Micromeritics ASAP 2020C (Norcross, GA, USA). The Micromeritics system was used to measure adsorption equilibrium between 1 mbar and 1.2 bar. The system has an accuracy of 0.15% in the loading measurement and a pressure accuracy of  $1.3 \times 10^{-7}$  mbar. A sample mass of 328.3 mg (zeolite 13X) or 477.8 mg (activated carbon) was used for these experiments. Prior to each experiment, the adsorbent was activated for 4 hours under vacuum (5  $\mu$ bar) at 350°C (zeolite 13X) or 200°C (activated carbon).

## 2.2 Micro Dynamic Column Breakthrough Apparatus

The  $\mu$ DCB system was built into a SRI 8610C gas chromatograph (GC) equipped with a thermal conductivity (TCD) detector. The integration required minor modifications to the GC hardware and the overall system schematic is shown in Fig. 1. Photos of the apparatus are shown in the Supporting Information. The internal plumbing of the GC was directed to allow an external mass flow controller (MFC), with a control range of 0.125 – 25.000 sccm, to meter the flow through the reference arm of the TCD. Adsorbate and purge gases were delivered to the  $\mu$ DCB bed through an 1/8" Swagelok bulkhead compression fitting that was installed in a hole drilled through the oven wall. The feed end of the bed was connected to the opposite side of the bulkhead connector and the exhaust of the bed was connected to the GC piping that led to the detector array. The outlet of the TCD was connected to a 1/8" Swagelok bulkhead connector that was installed in a hole drilled through the oven wall. The external connection of the bulkhead connector was connected to a length (approx. 2 to 10 meters) of 1/4" OD plastic tubing which delivered the analysis gas to an Alicat mass flow meter, MFM-1, with a 0 – 100.00 sccm measurement range.

Precise flow measurement and control is of critical importance to the application

[30]. The demands of working with small quantities of adsorbent required that the mass flow rates for the purge and analysis gases be known precisely; that the two gas flow rates be as equal as possible; and that the switch between the purge and adsorbate gases be reproducible, relatively instantaneous, and offer a smooth transition from one gas to the other. Of additional importance is the extra-column volume upstream of the bed. The upstream volume from the valve to the bed should be fully swept so as to avoid the complications associated with stranded pockets of gas which can complicate the analysis of the breakthrough curves [31]. To meet these requirements, a Bronkhorst Mini-Cori M12 coriolis mass flow meter ( $200 \pm 0.02$  g/hr) was installed upstream of the adsorbate gas mass flow controller, MFC-2. MFC-1 and MFC-2 mass flow controllers (Alicat) were used to control the delivery rate for the various gases but the signal from the coriolis mass flow meter upstream of MFC-2 was used as the true flow value. A flow-matching step was carried out to ensure that the flow rates for both MFC-1 and MFC-2 were equal. This procedure entailed flowing the adsorbate gas (MFC-2) through the system until MFM-1 read a constant value. Once the measured flow rate and composition of the system was constant, the valve was switched. A deviation in the signal for MFM-1, before and after the valve switch, was indicative of a mismatch in flow rate between MFC-1 and MFC-2 and, typically, the set point for MFC-1 was adjusted to match the flow rate delivered by MFC-2. The tubing placed upstream of MFM-1 facilitated a tuning sequence that was used to ensure that the mass flow rates for MFC-1 and MFC-2 were equal. The sequence began by actuating the switching valve to direct the gas from MFC-2 to flow through the test system (which was equipped with an empty bed). When the flow rate reported by MFM-1 was stable the switching valve was actuated to direct the gas from MFC-1 to flow through the test system. Any change in the flow rate reported by MFM-1 in the period of time directly after the valve was switched was related to a mismatch in the flow rate between MFC-2 and MFC-1. The flow rate for MFC-1 was increased or decreased depending on the direction of the difference and the sequence repeated until MFM-1 no longer registered a measurable difference between the flow rates from MFC-2 and MFC-1.

It should be mentioned that the signal output from MFM-1 is a function of both the flow rate and of the composition of the gas stream. If the flow rate and gas composition are changing simultaneously then a complicated calibration adjustment is required to correct the MFM signal so that the true flow rate can be derived. The calibration can be laborious and lead to serious measurement errors [30]. To avoid this requirement and to maintain a constant gas composition at MFM-1, a 2 – 10 meter length of tubing (depending on the adsorbent-adsorbate system) was placed upstream of the flow meter and downstream of the detector. It is worth noting that the flow wave in an adsorption or desorption experiment reaches MFM-1 instantaneously, regardless of the piping length [32]. This tubing created a reservoir of gas sufficient to maintain a constant gas composition at MFM-1 while the secondary gas travelled through the  $\mu$ DCB system. The miniaturization of the system makes the volume of the tubing manageable. Eventually the secondary gas did displace all of the initial gas in the tubing, and MFM-1 would signal this change in composition, but not before a stable flow trend was achieved. This design feature was instrumental in allowing the desorption flow curves to be collected in the absence of the complicating effects of changing gas composition.

To minimize the flow surge that inevitably accompanies a flow-switching event, several design features were implemented. Firstly, neither MFC-1 nor MFC-2 were dead-ended or shut-off during the experiment but instead continuously delivered gas at their set points. This feature eliminated the flow surge or flow dip that happens when an MFC has to adjust from zero flow to a set flow. A pneumatically-driven VICI 6-port valve was plumbed so that it had two common outlets. In its de-energized state the flow from MFC-1 was directed to the bed and the flow from MFC-2 was directed to vent. Conversely, when the valve is energized the flow from MFC-2 is directed to the bed and MFC-1 is directed to vent. This configuration required five of the six ports and the sixth, unused port was capped. The internal machining of the valve body ensures that the plenum space in the common ports is purged completely when the valve is switched. Ideally, a 4-port switching valve would be used instead of the 6-port



valve.

A manual back-pressure regulator was placed before the vent so that pressure downstream of both MFM-1 and MFM-2 could be matched to within 69.0 Pa,g (0.01 psig). The pressure sensors internal to the Alicat flow instruments facilitated this procedure. Pressure balancing was required to account for the pressure drop across the adsorbent bed. With both mass flow controllers providing the same flow, at the same backpressure, a smooth transition from one gas to another was realized. Pressure balancing was carried out for both adsorption and desorption experiments because the pressure drop across both the bed and the regulator are influenced by the composition of the gas stream.

To ensure repeatable flow switching times and to ensure that the flow switching event was synchronous with the GC data log, a relay internal to the GC was used to trigger the external VICI 6-port valve. The internal GC relay was wired to an external DC-DC solid-state relay which was used to trigger the direct-acting, 3-way solenoid which drove the pneumatic actuator for the VICI 6-port valve. Using a relay internal to the GC allowed the actuation of the external valve to be programmed into the GC software and actuated automatically at the required times. The solenoid valve was connected to a tank of helium and charged to a pressure of 7.9 bar (100 psig). The lower density of helium compared to compressed air facilitated a faster and more reproducible valve actuation event.

The  $\mu$ DCB bed housing was assembled from Swagelok VCR fittings. The bed consisted of four elements. Two SS-4-VCR-6-200 bodies were connected using a SS-4-VCR-CG coupler with a 20  $\mu$ m snubber frit installed between the glands of the mating parts. One of the bodies was drilled through to 11/64". Once all four parts were assembled, a quantity of adsorbent ( $\approx$  200 mg) was lightly tap-packed into the drilled-through body. This tap packing was a necessary step to ensure the integrity of the bed because the beds were installed horizontally into the oven. Vertical placement would have been preferred, but geometric constraints in the oven precluded this configuration. The tip of a thermocouple was nested in the leak port of the VCR coupling and wrapped

with fiberglass webbing. This modification did not influence the control of the GC, but monitoring the thermocouple temperature was necessary to understand when the bed housing had reached the air temperature reported by the GC. This temperature was monitored during the experiment and remained at a constant set point temperature. The large thermal mass of the bed housing took much longer to heat and to cool compared to the air in the oven.

A second bank of mass flow controllers (Alicat) was used to make binary mixtures. A combined flow of 200 sccm from MFC-4 and MFC-5 were fed into a 50 mL stainless steel blending tank to accomplish the complete mixing of the two gas streams. A typical  $\mu$ DCB experiment used  $\approx 5$  sccm of flow, and so a slipstream was provided to the 3-way valve that fed MFC-2 and the excess flow from MFC-4 and MFC-5 was vented through a back-pressure regulator that was set to 4.46 bar (50 psig).

**TCD Calibration:** A thermal conductivity detector (TCD) measures the difference between the thermal conductivities of a reference and an unknown (or analysis) gas. The TCD was chosen in this study due to its application in gas chromatography and use in small scale experiments. For small changes in gas composition, the output of the TCD can be assumed to be linear. In the  $\mu$ DCB experiments, the adsorbate concentration in the measurement arm of the TCD traverses very large concentration changes, especially when pure gases are being used. Most importantly though, the thermal conductivity of many common gas mixtures are not linear functions of composition [33–36]. The TCD signal is dependent on the gas mixture and composition, flow rate (in both the reference and analyzing cells), TCD block temperature and filament power [34]. Before a series of experiments began, the TCD signal was calibrated as a function of gas composition at a fixed reference gas flowrate (20 sccm for this study). A gas mixture was prepared using MFC-4 and MFC-5 and the mixture was fed to the TCD until the TCD signal stabilized. The data for a series of fourteen gas mixtures were conditioned in this way, which provided an adequate description of the TCD response over a wide range of mole fractions of adsorbate/purge gas. This calibration curve was used to convert the reported TCD signal in  $\mu$ V values to the mole fraction

of the adsorbate. An example TCD calibration is shown in Fig. 2 for  $\text{N}_2/\text{He}$  at a TCD block temperature of  $80^\circ\text{C}$  and He reference flow of 20 sccm. The calibration is shown as a normalized signal (see Fig. 2b) to include the effects of flowrate through the analyzing arm of the TCD. As seen in Fig. 2a, the normalized TCD signal increases in a non-linear fashion as a function of  $y_{\text{N}_2}$ . These trends were fitted to a variety of empirical equations to calculate the corresponding mole fraction from the normalized TCD signal. These figures are similar for the other gas mixtures used in this study and can be found in the Supporting Information along with all the empirical equations used to estimate the mole fractions.

**Blank Experiments:** The extra-column volume in the  $\mu\text{DCB}$  system was substantial compared to the volume of adsorbent present. To account for the accumulation of gas in the extra-column volume, and the fluid or void volume within the column, blank experiments were run at conditions identical to the adsorption experiments. The blank experiments used an equivalent empty VCR bed housing.

**Sample Mass:** The mass of the activated sample ( $m_{\text{ads}}$ ) needed to be known precisely and so the tare weight of the empty housing, purged with helium, was measured on a 0.1 mg analytical balance. The tare weight of the bed housing included two 1/8" Swagelok plugs that are connected to the inlet and outlet of the housing to prevent air from entering the housing. The empty housing was then filled with a quantity of adsorbent, activated *in situ* in the GC, and cooled under helium to  $30^\circ\text{C}$ . The exhaust of the bed was disconnected from the GC piping and plugged with the 1/8" fittings. The feed end of the bed was similarly dismantled and plugged. Using this procedure, air was largely excluded from entering the bed which preserved the sample in its activated state under helium. The entire bed was measured again on the 0.1 mg analytical balance and the difference between the tare and sample masses was the quantity of adsorbent (on a dry basis) under study. The activated adsorbent masses were measured to be 238.9 mg for zeolite 13X and 180.2 mg for activated carbon. This results in approximate bulk densities of 0.609 and 0.459 g/mL for zeolite 13X and activated carbon, respectively ( $V_{\text{col}} \approx 0.392 \text{ mL}$ ).

**Pycnometric Adjustment:** The presence of adsorbent in the bed housing changes the blank volume in the system. As a result, the measured blank response will overpredict the fluid accumulation in the system when adsorbent is present. To correct for the volume occupied by the framework of the solid, the pycnometric (skeletal) density ( $\rho_{\text{sk}}$ ) of the adsorbent was measured. The pycnometric density of the adsorbent was measured using the Micromeritics ASAP 2020C. An empty reference tube was evacuated, filled with helium, and weighed on a 0.1 mg analytical balance to measure its tare weight. This reference tube was mounted to the instrument and the freespace of the tube was measured several times at 30°C and the values were averaged. A known quantity of adsorbent was then added into the same tube, activated *in situ* on the instrument, cooled to 30°C and, again, the freespace was measured several times. The mass of the activated sample and the difference in the measured freespace between the empty reference tube and the tube including adsorbent yield the skeletal density of the adsorbent. This density can be used to correct the blank volume of the  $\mu$ DCB because the dry weight of adsorbent in the  $\mu$ DCB column is known. The values are equal to 2.54 and 2.00 g/mL for zeolite 13X and activated carbon, respectively. It is worth noting that using helium to measure the skeletal volumes has its challenges. Assuming helium is non-adsorbing can lead to the estimation of skeletal volume [37, 38]. This can be problematic for high pressure measurements, but is not of concern for low pressures such as the ones studied here.

**Blank Response:** A blank experiment at 30°C with 100 mol% N<sub>2</sub> (in He) is shown in Fig. 4 with a schematic of the blank in Fig. 3. The TCD trace in Fig. 4a highlights the need for precise control over all process variables because the transition time from pure helium to pure N<sub>2</sub> is only a matter of seconds, whether transitioning from He to N<sub>2</sub>, or from N<sub>2</sub> to He. Note that when the signals are plotted without the calibration curve, they are not symmetric. A blank column should not show any asymmetry between He or N<sub>2</sub> as test gases. This is already an indication that the TCD signal has a non-linear dependency on mole fraction. While not entirely necessary, having a single, continuous mass flow rate somewhat simplifies the mass balance calculations. When

the calibration curve is applied to the TCD signal the adsorption and desorption curves can be plotted together (Fig. 4b) using the valve trigger time as  $t = 0$  for each curve. The two curves intersect at their midpoints which indicates that the TCD calibration curve is able to accurately transform a mV response into a molar composition and give confidence for use with a packed bed. Figure 4c plots the mole fraction of  $N_2$  ( $y_{N_2}$ ) for adsorption and  $1 - y_{N_2}$  for desorption to show that both signals overlap. This is further confirmation of the correct calibration and that the instrument is able to capture the correct dynamics of a blank experiment. It is important to emphasize that the goal of the current work is to obtain equilibrium data from DCB experiments. If there is a need either to obtain kinetic data or to compare the experimental results with that of simulations, the dynamics of the blank volume has to be characterized [32, 39].

**Typical Experiment:** Adsorbents were activated *in situ* and cooled to the analysis temperature under He. Once at the analysis temperature (as measured by the thermocouple connected to the  $\mu$ DCB bed) was constant, MFC-2 was pressure balanced using the back pressure regulator (BPR) to match the pressure displayed by MFC-1. Both flow instruments indicate the pressure upstream of the instruments.

The GC was programmed with a 35 min sequence (for an inlet flow of 5 sccm) that involved two valve actuations. An adsorption/desorption sequence collected the He baseline signal for 5 min before the valve was switched to allow the adsorbate gas ( $N_2$ ) to saturate the bed for a period of 15 min. The valve was then returned to its original position to allow He to displace the  $N_2$  from the bed. The desorption step was 15 min long to ensure that the bed has desorbed all of the  $N_2$  before the next experiment was started. Pressure balancing using the BPR-1 was carried out at the 1 min mark and at the 12 to 15 min mark during the experiment. For more strongly adsorbing systems, these timestamps were extended to ensure that complete saturation and regeneration was achieved, along with the gas composition change in the tank before MFM-1.

Figure 5 shows the mole-fraction-calibrated TCD trace for a 100 mol%  $N_2$ /He experiment on zeolite 13X at 30°C. Data was collected at a rate of 10 Hz giving a time resolution of 100 ms. Again, the composition trace displays a sharp transition

for the adsorption experiment, but a more gradual transition in the desorption curve. The MFM-1 data is also shown in Fig. 5. The MFM signal shows both the flow drop associated with the adsorption event (Fig. 5a) and the flow-surge resulting from the desorption of N<sub>2</sub> from the adsorbent (Fig. 5b). Sufficient time was allowed for the effluent flowrate (measured by MFM-1) to return to the inlet flowrate (controlled by MFC-1 or MFC-2) and the effluent composition to be identical to that at the inlet allowing the closure of the transient mass balance.

**Important Design Considerations:** The inlet flowrate,  $Q_{\text{in}}$ , was an important design parameter in the  $\mu$ DCB experiments. Specifically, if the inlet flow was too large, the breakthrough risks being under kinetic control. This is also a parameter in the design of zero-length column (ZLC) experiments [25]. A nondimensional parameter,  $L$ , can be introduced to determine if a ZLC experiment is in equilibrium or kinetic control:

$$L = \frac{1}{3} \frac{Q_{\text{in}}}{H_i V_{\text{ads}}} \frac{R_p^2}{D_{p,i}} \quad (1)$$

where  $H_i$  is the dimensionless Henry constant of adsorbate  $i$ ,  $V_{\text{ads}}$  is the adsorbent volume, and  $\frac{D_{p,i}}{R_p^2}$  is the pore diffusional time constant. If  $L \leq 1$ , the system is under equilibrium control. Therefore, the maximum inlet flowrate ( $Q_{\text{in,max}}$ ) should follow the relationship:

$$Q_{\text{in,max}} \leq 3LH_i V_{\text{ads}} \frac{D_{c,i}}{R_p^2} \quad (2)$$

Note that this requirement, borrowed from the ZLC literature, provides an estimation of the flowrates to be enforced. All flowrates in this study were chosen to be less than  $Q_{\text{in,max}}$ . At 30°C for the zeolite 13X and activated carbon beds in this study,  $Q_{\text{in,max}}$  is  $\approx 13.0$  sccm for N<sub>2</sub>.

The pressure drop across the  $\mu$ DCB system was also very important. Specifically, the pressure drop needed to be as small as possible. This appeared to be a more significant problem than in larger systems. The best column performance was found in systems with a similar pressure drop to a blank VCR fitting ( $\approx 0.06$  bar). At pressure drops greater than  $\approx 0.1$  bar, the calculated adsorption and desorption equilibrium

loadings would no longer be the same value. The pressure drop across the  $\mu$ DCB was reduced by a loose tap-packing of adsorbent into the VCR fitting.

### 3 Mass Balances and Error Analysis

#### 3.1 Experimental Mass Balances

To obtain equilibrium data from the  $\mu$ DCB, two separate experiments must be performed: a “blank experiment”, which is performed through an empty Swagelok VCR fitting, and a “composite response”, which is the column/adsorbent response plus the blank response through an equivalent Swagelok VCR fitting.

The blank experiment is performed at a uniform temperature, pressure, inlet flow and composition without any adsorbent in the VCR fitting. Although these conditions need not strictly be the same as the composite experiment. For the sake of visualization, it is convenient that the conditions for the blank and composite experiments are the same. This approach was taken throughout this study. The mass balance for a blank experiment can be written as:

$$\text{Input} - \text{Output} = \text{Accumulation} \quad (3)$$

which can be written as:

$$\int_0^{t_\infty} Q_{\text{in}} C_{i,\text{in}} dt - \int_0^{t_\infty} Q(t) C_i(t) dt = V_{\text{col}} C_{i,\text{in}} \quad (4)$$

where  $Q_{\text{in}}$  and  $Q(t)$  are the inlet and outlet volumetric flow rates, while  $C_{i,\text{in}}$  and  $C_i(t)$  are the corresponding concentrations of component  $i$ . Assuming the gas is ideal, Eqn. 4 can be written as:

$$\int_0^{t_\infty} Q_{\text{in}} \frac{y_{i,\text{in}} P}{RT} dt - \int_0^{t_\infty} Q(t) \frac{y_i(t) P}{RT} dt = V_{\text{col}} \frac{y_{i,\text{in}} P}{RT} \quad (5)$$

Assuming isothermal operation and a negligible pressure drop; the above equation can be simplified to:

$$\bar{t}_{\text{blank,ads}} = \int_0^{t_\infty} \left( 1 - \frac{Q(t)y(t)}{Q_{\text{in}}y_{\text{in}}} \right) dt = \frac{V_{\text{col}}}{Q_{\text{in}}} \quad (6)$$

where  $\bar{t}_{\text{blank}}$  is the blank time, i.e. the average time required for an adsorbent molecule to travel through the blank volume. Now let us consider an adsorption experiment where a mass of  $m_{\text{ads}}$  is placed in the same column in which the blank was measured. Under this condition, the mass balance will take the form:

$$\int_0^{t_\infty} Q_{\text{in}} C_{i,\text{in}} dt - \int_0^{t_\infty} Q(t) C_i(t) dt = (V_{\text{col}} - V_{\text{sk}} - V_{\text{s}}) C_{i,\text{in}} + V_{\text{s}} \rho_{\text{m,s}} \quad (7)$$

The first term on the right hand side represents the accumulation in the fluid phase and the second term indicates the accumulation in the adsorbed phase. Further,  $V_{\text{sk}}$  represents the skeletal volume as measured in the helium pycnometric experiment,  $V_{\text{s}}$  represents the volume of “adsorbed phase” and  $\rho_{\text{m,s}}$  denotes the molar density of the adsorbed phase. Note that  $V_{\text{sk}}$  can be written as:

$$V_{\text{sk}} = \frac{m_{\text{ads}}}{\rho_{\text{sk}}} \quad (8)$$

where  $\rho_{\text{sk}}$  is the skeletal density of the adsorbent. Here, Eqn. 7 can be written as:

$$\int_0^{t_\infty} Q_{\text{in}} C_{i,\text{in}} dt - \int_0^{t_\infty} Q(t) C_i(t) dt = \left( V_{\text{col}} - \frac{m_{\text{ads}}}{\rho_{\text{sk}}} \right) C_{i,\text{in}} + V_{\text{s}} (\rho_{\text{m,s}} - C_{\text{in}}) \quad (9)$$

The second term on the right hand side is the excess amount adsorbed. For systems at low pressure  $\rho_{\text{m,s}} \gg C_{\text{in}}$ , and hence the equation simplifies to:

$$\int_0^{t_\infty} Q_{\text{in}} C_{i,\text{in}} dt - \int_0^{t_\infty} Q(t) C_i(t) dt = \left( V_{\text{col}} - \frac{m_{\text{ads}}}{\rho_{\text{sk}}} \right) C_{i,\text{in}} + m_{\text{ads}} q_i^* \quad (10)$$

where  $q_i^*$  is the absolute amount adsorbed in equilibrium with the fluid phase concentration  $C_{i,\text{in}}$ . Since the thermal mass of the fitting is high we assume that the system is isothermal and that the pressure drop is negligible. These can be confirmed by measurements of  $T$  and  $\Delta P$ . Eqn. 10 can be written as:

$$\bar{t}_{\text{comp,ads}} = \int_0^{t_\infty} \left( 1 - \frac{Q(t)y(t)}{Q_{\text{in}}y_{\text{in}}} \right) dt = \left( V_{\text{col}} - \frac{m_{\text{ads}}}{\rho_{\text{sk}}} \right) \frac{1}{Q_{\text{in}}} + \frac{RT m_{\text{ads}} q_i^*}{P y_{\text{in}} Q_{\text{in}}} \quad (11)$$



Note that the term represented by the integral is measured from the experiment. Equation 11 can be written as:

$$\bar{t}_{\text{comp,ads}} = \left[ \bar{t}_{\text{blank,ads}} - \bar{t}_{\text{pync}} \right] + \frac{RTm_{\text{ads}}q_i^*}{Py_{\text{in}}Q_{\text{in}}} \quad (12)$$

where  $\bar{t}_{\text{pync}}$  is the pyncnometric correction and is defined as:

$$\bar{t}_{\text{pync}} = \frac{m_{\text{ads}}}{\rho_{\text{sk}}} \frac{1}{Q_{\text{in}}} \quad (13)$$

These terms can be rearranged to obtain the adsorbate loading from an adsorption experiment:

$$q_{i,\text{ads}}^* = \frac{Py_{i,\text{in}}}{RT} \frac{Q_{\text{in}}}{m_{\text{ads}}} \left[ \bar{t}_{\text{comp,ads}} - \bar{t}_{\text{blank,ads}} + \bar{t}_{\text{pync}} \right] \quad (14)$$

For a desorption experiment, where the adsorbate is originally in equilibrium at  $C_{i,\text{in}}$  in the column, the equilibrium loading can be described as:

$$q_{i,\text{des}}^* = \frac{Py_{i,\text{init}}}{RT} \frac{Q_{\text{init}}}{m_{\text{ads}}} \left[ \bar{t}_{\text{comp,des}} - \bar{t}_{\text{blank,des}} + \bar{t}_{\text{pync}} \right] \quad (15)$$

where

$$\bar{t}_{\text{comp,des}} = \int_0^{t_\infty} \left( \frac{Q(t)y(t)}{Q_{\text{init}}y_{\text{init}}} \right) dt = \left( V_{\text{col}} - \frac{m_{\text{ads}}}{\rho_{\text{sk}}} \right) \frac{1}{Q_{\text{init}}} + \frac{RTm_{\text{ads}}q_i^*}{Py_{\text{init}}Q_{\text{init}}} \quad (16)$$

and

$$\bar{t}_{\text{blank,des}} = \int_0^{t_\infty} \left( \frac{Q(t)y(t)}{Q_{\text{init}}y_{\text{init}}} \right) dt = \frac{V_{\text{col}}}{Q_{\text{init}}} \quad (17)$$

Note that Eqns. 14 and 15 can be used for either a single-component or multicomponent experiment. When multicomponent experiments are involved, the measured loading correspond to the competitive/cooperative loading for a given component. In a system with no hysteresis, the loading measured in the adsorption and desorption experiments should yield the identical values.

## 3.2 Error Analysis

An error analysis was performed to determine the significance of the calculated data. The uncertainty associated with a variable  $\gamma$  in a function  $f$ ,  $\delta f$ , is given by:

$$\delta f = \left| \left( \frac{\partial f}{\partial \gamma} \right) \delta \gamma \right| \quad (18)$$

where  $\delta \gamma$  is the uncertainty of  $\gamma$ .

There are eight variables in the  $\mu$ DCB apparatus that add to the uncertainty in the calculation of the equilibrium loading ( $q^*$ ):  $m_{\text{ads}}$ ,  $T$ ,  $P$ ,  $\rho_{\text{sk}}$ ,  $y_{\text{in}}$ ,  $Q_{\text{in}}$ ,  $y(t)$  and  $Q(t)$ . The measurement of both  $y$  and  $Q$  at the inlet and outlet are split into two separate sets of variables since they are measured with different instruments. The sum of all of these errors yields the total system (plus/minus) error for the equilibrium loading:

$$\delta q^* = \sum_i \left| \left( \frac{\partial q^*}{\partial \gamma_i} \right) \delta \gamma_i \right| \quad (19)$$

The uncertainties associated with these terms are shown in Table 1. The error propagation equations and derivations are shown in the Supporting Information. The error bars shown in all figures with  $\mu$ DCB equilibrium loading calculations are from these error propagation calculations.

## 4 Results and Discussion

### 4.1 Volumetric Single-Component Equilibrium

The equilibrium data for  $\text{N}_2$ ,  $\text{CH}_4$  and  $\text{CO}_2$  on zeolite 13X and for  $\text{N}_2$  and  $\text{CH}_4$  on activated carbon was measured using the Micromeritics ASAP 2020C (Norcross, GA, USA). The  $\text{N}_2$ ,  $\text{CH}_4$  and  $\text{CO}_2$  data is shown in Fig. 6. The  $\text{N}_2$  and  $\text{CH}_4$  isotherms for zeolite 13X are essentially linear at all temperatures and pressures, which allows them to be reasonably approximated with a linear isotherm:

$$q_i^* = K_i P_i \quad (20)$$

with  $K_i$  being the temperature dependent Henry constant. The temperature dependence of  $K_i$  is given by the Van't Hoff relationship:

$$K_i = K_{0,i} \exp \left( \frac{-\Delta H_{\text{b},i}}{RT} \right) \quad (21)$$

where  $K_{0,i}$  is the Henry constant prefactor, and  $\Delta H_{b,i}$  is the heat of adsorption of component  $i$ . The adsorption of  $\text{CO}_2$  on zeolite 13X was described using a dual-site Langmuir (DSL) isotherm.  $\text{CH}_4$  equilibrium data on zeolite 13X was also fitted with a DSL isotherm to better estimate competition between  $\text{CH}_4$  and  $\text{CO}_2$  using an equal-energy sites (EES) approximation [8]. The dual-site Langmuir isotherm is shown below:

$$q_i^* = \frac{q_b^{\text{sat}} b_i P_i}{1 + \sum_j^{n_{\text{comp}}} b_j P_j} + \frac{q_d^{\text{sat}} d_i P_i}{1 + \sum_j^{n_{\text{comp}}} d_j P_j} \quad (22)$$

where  $q_b^{\text{sat}}$  and  $q_d^{\text{sat}}$  are the saturation capacities of the  $b$  and  $d$  sites, respectively and  $b_i$  and  $d_i$  are the temperature dependent nonlinearity constants. The temperature dependence of  $b_i$  and  $d_i$  are given by:

$$b_i = b_{0,i} \exp\left(\frac{-\Delta H_{b,i}}{RT}\right) \quad (23)$$

$$d_i = d_{0,i} \exp\left(\frac{-\Delta H_{d,i}}{RT}\right) \quad (24)$$

where  $b_{0,i}$  and  $d_{0,i}$  are the nonlinearity constant prefactor of component  $i$  on sites  $b$  and  $d$ , and  $\Delta H_{d,i}$  is the heat of adsorption of component  $i$  in second adsorption site  $d$ . The isotherms  $\text{N}_2$  and  $\text{CH}_4$  on activated carbon were fitted to single-site Langmuir (SSL) isotherms:

$$q_i^* = \frac{q_b^{\text{sat}} b_i P_i}{1 + \sum_j^{n_{\text{comp}}} b_j P_j} \quad (25)$$

The isotherm parameters for all systems are listed in Table 2.

## 4.2 Single-Component Breakthrough Experiments

Single component breakthrough experiments were performed on zeolite 13X for  $\text{N}_2$  and  $\text{CH}_4$  at  $\approx 0.96$  bar and 30, 40 and 50°C. A summary of the breakthrough experiments is shown in Table 3. All experiments were performed at 5.3 sccm (standard conditions are:  $T_{\text{std}} = 0^\circ\text{C}$  and  $P_{\text{std}} = 1.01325$  bar).

The results of the single-component  $\text{N}_2$  adsorption and desorption breakthrough experiments at  $30^\circ\text{C}$  on zeolite 13X are shown in Fig. 7. The blank measurement is shown in black, the pycnometrically corrected blank is shown in blue and the composite response is shown in red. Helium was used as a sweep gas and diluent for all single component breakthrough experiments. Helium was also the reference gas in the TCD for all single-component experiments. As seen in Fig. 7, the composite response always exits later than the pycnometrically corrected blank. The shaded areas in Fig. 7a and b are proportional to the accumulation in each experiment (between the blue and red curves). Although not essential, a blank experiment was performed for every adsorbate and set of conditions studied. From Fig. 7, it is seen that as the composition of  $\text{N}_2$  decreases, that the composite adsorption breakthrough curves seem more dispersed, while all sharing the average retention time at  $\approx 40$  seconds. This is a common phenomenon observed for adsorbates with a linear isotherm [12, 13].

The adsorption and desorption breakthrough curves are plotted as a normalized molar flow ( $y(t)Q(t)/[y_{\text{in}}Q_{\text{in}}]$ ), a combination of the effluent  $\text{N}_2$  mole fraction,  $y(t)$ , and flow curves,  $Q(t)$ , divided by the inlet (or initial for desorption) mole fraction ( $y_{\text{in}}$ ) and flow ( $Q_{\text{in}}$ ), to show how  $\text{N}_2$  accumulates in the adsorbent. For adsorption, this quantity goes to a value of 1 when breakthrough is finished. During an adsorption experiment the flow at the outlet of the column will decrease to the carrier/inert flowrate (in this case He) as the adsorbate (in this case  $\text{N}_2$ ) adsorbs into the adsorbent. This is seen in Fig. 5b. When the adsorbate breaks through the packed bed, the flow increases to the inlet value with the adsorbate mole fraction. This yields a breakthrough curve (Fig. 7a) that is similar, but not equal to, the mole fraction breakthrough curve (see Fig. 5a) [12]. For desorption, notice that initially the normalized molar flow is above 1; this means that the flow rate of  $\text{N}_2$  increases above the inlet flowrate,  $Q(t) > Q_{\text{in}}$ , during the first few seconds of desorption (until  $\approx 16$  seconds). This is due to the desorption of  $\text{N}_2$ , that contributes to an increased flowrate. After the initial flow spike, the flow decreases as  $\text{N}_2$  leaves the bed and approaches zero as both  $Q(t)$  returns to the inlet flow value, and as  $y(t)$  approaches zero. When the desorption normalized molar

flow goes to zero, desorption is complete. Single component adsorption and desorption breakthrough experiments were also performed at 40 and 50°C for 25, 50 and 100 mol% N<sub>2</sub> in He, but are shown in the Supporting Information.

Using either Eqn. 14 for an adsorption experiment, or Eqn. 15 for a desorption experiment, the adsorbate loading can be calculated. These values are shown in Fig. 6 together with the volumetrically collected equilibrium data and the linear isotherm fit. Tabulated equilibrium data is given in Table 3. As seen in Fig. 6, the adsorption data (hollow markers) and desorption data (solid markers) from the  $\mu$ DCB measurements are within 5% of the volumetrically collected data. The error associated with the  $\mu$ DCB calculated loadings is small, generally 4 – 5% of the calculated adsorption/desorption loading.

To demonstrate the repeatability of the  $\mu$ DCB system, a series of 100 mol% N<sub>2</sub>/He experiments were performed at 30°C, 0.95 bar and 5.3 sccm. Five repetitions of an adsorption and desorption breakthrough experiment were performed, which resulted in ten estimates for the N<sub>2</sub> equilibrium loading at 30°C and 0.95 bar. These dimensionless molar flow curves are shown in Fig. 8. As seen in Fig. 8, the five repeated composite adsorption (Fig. 8a) and desorption (Fig. 8b) experiments are virtually indistinguishable from each other. The mass balances were solved, and the calculated equilibrium data is shown with the isotherm and volumetrically collected data (at 30°C) in Fig. 8c. In Fig. 8c, the blue squares are adsorption equilibrium loadings, the green triangles are desorption equilibrium loadings and the black diamond is the average of all ten adsorption and desorption loadings ( $\bar{q}_{N_2}^* = 0.3377$  mol/kg). As seen in Fig. 8c, the  $\mu$ DCB is highly repeatable, and agrees very well with the volumetrically collected data. The error bars for the adsorption and desorption equilibrium loadings are estimated with Eqn. 19, which represents the largest possible deviation from the measured loading if all measurements are incorrect by their inherent uncertainty. These values range between  $4.81 \times 10^{-3}$  and  $1.02 \times 10^{-2}$  mol/kg. The standard experimental error was calculated to be  $1.41 \times 10^{-3}$  mol/kg, approximately three times less than the lowest estimate from error propagation, showing that experimental variability is less than the

estimated error propagation. These results give confidence that the  $\mu$ DCB is able to accurately and precisely calculate the equilibrium loading.

Single-component  $\text{CH}_4$  adsorption and desorption experiments were also performed to determine if the  $\mu$ DCB apparatus was able to measure adsorption equilibrium and column dynamics of different species. The  $\text{CH}_4$  breakthrough experiments at  $30^\circ\text{C}$  for 25, 50 and 100 mol%  $\text{CH}_4$  in He are shown in the Supporting Information. Many of the same observations were noticed for  $\text{CH}_4$  as were noticed for  $\text{N}_2$ . As seen in Fig. 6, the  $\text{CH}_4$  equilibrium data is essentially linear over the pressure and temperature range studied. Therefore, the same adsorption breakthrough time is observed with  $\text{CH}_4$  at  $30^\circ\text{C}$  on zeolite 13X for all three compositions studied (25, 50 and 100 mol% in He). Since  $\text{CH}_4$  is stronger than  $\text{N}_2$  on zeolite 13X,  $\text{CH}_4$  breaks through later in time than  $\text{N}_2$ . The  $\text{CH}_4$  loadings were calculated using Eqn. 14 and Eqn. 15 for an adsorption and desorption experiment, respectively. The error of these values are typically between 2–4% of the measurement and within 5% of the volumetrically collected  $\text{CH}_4$  data. As seen in Fig. 6d, the  $\mu$ DCB measurements are in good agreement with the volumetrically collected data. The single-component  $\text{CH}_4$  equilibrium data for zeolite 13X is given in Table 3.

Single component breakthrough experiments were also performed on an activated carbon (Calgon BPL 4x10 CAS#7440-44-00), for 25, 50 and 100 mol% mixtures of  $\text{N}_2/\text{He}$  and  $\text{CH}_4/\text{He}$  at  $\approx 0.95$  bar and 30, 40 or  $50^\circ\text{C}$ . These experiments were performed to determine whether this method would be able to predict consistent and accurate equilibrium data for different types of adsorbent materials. Overall, the same findings were found for activated carbon as were found for zeolite 13X. The adsorption/desorption breakthrough curves are shown in the Supporting Information. The equilibrium data for both  $\text{N}_2$  and  $\text{CH}_4$  is shown in Fig. 6 as hollow and solid diamonds for adsorption and desorption, respectively. Tabulated equilibrium data is given in Table 4. As before with zeolite 13X, the  $\mu$ DCB adsorption and desorption measured equilibrium loadings agree well with the volumetrically collected data for both  $\text{N}_2$  and  $\text{CH}_4$ . The error of  $\mu$ DCB measurements is similar to that of zeolite 13X, generally

between 2 – 4% of the measurement and within 5% of the volumetrically collected data.

### 4.3 Binary Breakthrough Experiments in the Absence of Competition

Due to the small amount of sample used, and the relatively fast experimental times, the  $\mu$ DCB has the potential to be a very rapid method to quantify multicomponent adsorption equilibrium. Mixtures of  $\text{CH}_4$  and  $\text{N}_2$  on zeolite 13X were chosen to study an ideal case of co-adsorption in the absence of adsorptive competition. Both  $\text{N}_2$  and  $\text{CH}_4$  exhibit a linear isotherm on zeolite 13X. Two adsorbates with linear isotherms typically do not show competitive adsorption [4]. Multicomponent  $\mu$ DCB experiments were still run as a binary mixture, but now with the reference helium, and helium carrier, replaced with another adsorbing gas. For example, for a  $\text{CH}_4/\text{N}_2$  binary experiment, the carrier could either be  $\text{CH}_4$  to measure the binary loading of  $\text{N}_2$ , or  $\text{N}_2$  to measure the binary loading of  $\text{CH}_4$ . This is different than what is usually done in the literature, where a ternary mixture is made with He, or  $\text{H}_2$ , as an inert sweep gas [8, 40–45]. Although uncommon, this method has been used previously to study equilibrium and kinetics of binary mixtures of gases [14]. This limitation arises owing to the decision to use a TCD instead of a multicomponent detector, such as a mass spectrometer. The use of an inert (such as helium) as a reference gas will not be able to distinguish between the two test gases ( $\text{N}_2/\text{CH}_4$ ), therefore the idea is to employ one of the test gases as the TCD reference gas. The change of the reference gas does change the TCD calibration (with respect to the analyzed gas), but the change also blinds the TCD to the carrier gas allowing for the analyzed gas to be measured in a competitive experiment. This does require two sets of experiments to complete a binary isotherm at a given temperature and pressure: one for each adsorbate in the mixture. The first set of experiments starts with a bed saturated with  $\text{N}_2$  (to measure  $\text{CH}_4$ ) and the second set starts with a bed initially saturated with  $\text{CH}_4$  (to measure  $\text{N}_2$ ). Therefore, for an “adsorption”

experiment, when the analyzed component adsorbs, the reference component is being desorbed from 100 mol% of the reference component to the feed composition. Likewise for a “desorption” experiment, when the analyzed component desorbs, the reference component is being adsorbed from the feed composition to 100 mol% of the reference component. This at times yields unusual molar flow curves for the light component in the binary mixture. Specifically for a desorption experiment, the effluent flow,  $Q(t)$ , can drop below the inlet flow,  $Q_{\text{in}}$ , which is the different from a single-component experiment. The opposite, where  $Q(t)$  increases higher than  $Q_{\text{in}}$ , is possible as well in an adsorption experiment; however, it is not seen in the normalized molar flow curves since the mole fraction is equal to zero at the coincident times. A sample set of experiments for an approximately 50/50 mol%  $\text{CH}_4/\text{N}_2$  mixture on zeolite 13X at 30°C and 0.95 bar is shown in Fig. 9. Binary mixtures of 25/75 and 75/25 mol%  $\text{CH}_4/\text{N}_2$  at 30°C and 0.95 bar were also performed, but are not shown in the main body of this paper. All other  $\text{CH}_4/\text{N}_2$  adsorption and desorption breakthrough curves are shown in the Supporting Information.

For the first set of multicomponent experiments on zeolite 13X,  $\text{CH}_4$  was measured while  $\text{N}_2$  was used as the TCD reference gas and is blinded. This means that the zeolite 13X bed was initially saturated with 100 mol%  $\text{N}_2$  at 0.95 bar and 30°C. In a  $\text{CH}_4/\text{N}_2$  mixture,  $\text{CH}_4$  is the heavy component, exhibiting a larger capacity on zeolite 13X than  $\text{N}_2$  at similar conditions (see Fig. 6). Since,  $\text{CH}_4$  is the heavy component, the adsorption and desorption breakthrough curves will qualitatively look similar to a single-component  $\text{CH}_4$  experiment [12, 14]. These curves are shown in Fig. 9a and b, for adsorption and desorption respectively. Due to the increase in flow on desorption, the normalized flow curves initially increase in Fig. 9b to about 20 seconds, where the flow starts to approach the feed flowrate of 5.3 sccm.

The  $\text{N}_2$  experiments are shown in Fig. 9c and d. These are separate experiments where the column was initially saturated with  $\text{CH}_4$  at 0.95 bar and 30°C with  $\text{CH}_4$  used as the TCD reference. Since  $\text{N}_2$  is the weaker component in the  $\text{CH}_4/\text{N}_2$  mixture, the effluent flow curves ( $Q(t)$ ) do not resemble a typical single-component experiment,



as explained earlier. Specifically,  $\text{CH}_4$  (the heavy component) seems to dictate the behavior of the effluent flow. The effluent flow curve for the 48.7/51.3 mol%  $\text{N}_2/\text{CH}_4$  experiment are shown in Fig. 9e and f, for adsorption and desorption, respectively. During adsorption, the flow in Fig. 9e initially increases, despite the fact the  $\text{N}_2$  is adsorbing into the column. This trend occurs since  $\text{CH}_4$  is being simultaneously desorbed and the quantity of  $\text{CH}_4$  desorbed is greater than the quantity of  $\text{N}_2$  adsorbed. This flow curve yields a  $\text{N}_2$  adsorption breakthrough curve that resembles a single-component desorption curve. Likewise for desorption in Fig. 9d,  $\text{N}_2$  is being desorbed while  $\text{CH}_4$  adsorbs. This yields a desorption molar flow curve that has a dip in the initial curve. When the  $\text{N}_2$  desorption experiment starts, the flow drops below  $Q_{\text{in}}$ , since  $\text{CH}_4$  is adsorbing (see Fig. 9f). This causes the initial molar flow curve of  $\text{N}_2$  to decrease and then increase slightly (never going above one) as  $\text{CH}_4$  breaks through the column. At this time, the  $\text{N}_2$  molar flow curve begins to decrease again as a typical single component desorption curve. While not shown in the main body of the paper, this becomes more pronounced as the composition of  $\text{N}_2$  decreases, or as the quantity of  $\text{CH}_4$  increases. In all measured light component breakthroughs (in the Supporting Information), the desorption normalized molar flow curve for the light component was always less than or equal to one. For a single component desorption, this value is initially greater than one, as flow increases during desorption, and then decreases as the mole fraction approaches zero and the flow returns to the feed flow.

Solving the adsorption (hollow markers) and desorption (solid markers) mass balances yields the expected single-component equilibrium values for both  $\text{N}_2$  and  $\text{CH}_4$ . These values are shown in Fig. 10a and are tabulated in Table 5. Both the  $\text{N}_2$  and  $\text{CH}_4$  predictions are virtually indistinguishable from the expected values, assuming single-component linear isotherms, except for the 100 mol%  $\text{CH}_4$  (in He) adsorption/desorption experiments, which fall slightly below the single-component isotherm prediction. Again, since both  $\text{N}_2$  and  $\text{CH}_4$  exhibit linear isotherms on zeolite 13X, the competitive loadings can be predicted with the single-component isotherms. The error associated with these measurements was  $\approx 2 - 5\%$  of the calculated  $\mu\text{DCB}$  load-

ing. These experiments confirm that the  $\mu$ DCB is able to measure binary equilibrium data accurately and precisely with the expected noncompetitive, ideal behavior. The four adsorption/desorption measurements for one gas in the binary mixture (Fig. 10a), and their associated blank measurements, could be measured comfortably in a single work-day ( $\approx 5 - 6$  hours).

#### 4.4 Competitive Binary Breakthrough Experiments

A series of  $\text{CH}_4/\text{N}_2$  experiments were then performed on activated carbon to determine if the  $\mu$ DCB apparatus was able to measure  $\text{CH}_4/\text{N}_2$  adsorptive competition. Unlike  $\text{CH}_4/\text{N}_2$  mixtures on zeolite 13X,  $\text{CH}_4$  and  $\text{N}_2$  can be expected to adsorb competitively on activated carbon due to the nonlinear trend of  $\text{CH}_4$  shown in Fig. 6. These experiments were performed as 25/75, 50/50 and 75/25 mol% mixtures of  $\text{CH}_4/\text{N}_2$  initially at  $30^\circ\text{C}$  and 0.95 bar. The adsorption and desorption breakthrough curves of all  $\text{CH}_4/\text{N}_2$  mixtures on activated carbon are shown in the Supporting Information. The calculated adsorption (hollow markers) and desorption (solid markers) equilibrium loadings of  $\text{N}_2$  and  $\text{CH}_4$  at  $30^\circ\text{C}$  are shown in Fig. 11a with IAST predictions as solid lines. Tabulated equilibrium data is given in Table 6. As seen in Fig. 11a, the  $\text{N}_2$  equilibrium loadings appear to follow the predictions from IAST. The calculated  $\text{N}_2$  loadings are all slightly less than the IAST predictions, but fall within the error bars. On the other hand,  $\text{CH}_4$  appears to compete non-ideally, with all adsorption and desorption equilibrium loadings above the IAST predictions.

The  $\text{CH}_4/\text{N}_2$  mixture (25/75, 50/50 and 75/25 mol%) experiments were repeated at  $40^\circ\text{C}$  and  $50^\circ\text{C}$  at 0.95 bar. This was partially initiated to demonstrate the ability of the  $\mu$ DCB to work at different temperatures and to examine if  $\text{CH}_4/\text{N}_2$  remains a nonideal system on activated carbon at different temperatures. The  $\mu$ DCB adsorption and desorption loadings are shown in Fig. 11b and c for  $40^\circ\text{C}$  and  $50^\circ\text{C}$ , respectively. At  $40^\circ\text{C}$  and  $50^\circ\text{C}$ ,  $\text{N}_2$  appears to remain ideal. Methane appears to become more ideal as the temperature increases from  $30^\circ\text{C}$  to  $50^\circ\text{C}$ .

These results are consistent with the literature. Kennedy *et al.* reported slight nonideal competition between CH<sub>4</sub> and N<sub>2</sub> on Xtrusorb A754 activated carbon at 30°C and 1.01 bar [46]. Specifically, Kennedy *et al.* found both CH<sub>4</sub> and N<sub>2</sub> exhibit a slightly positive deviation from ideality with CH<sub>4</sub> exhibiting a larger deviation. At higher pressures (4.05 bar), CH<sub>4</sub> could be considered ideal, while N<sub>2</sub> exhibits a larger positive deviation from ideality (than at 1.01 bar). Wu *et al.* found that for pitch-based activated carbon at 30°C and 1.00 bar, both CH<sub>4</sub> and N<sub>2</sub> were ideal [47]. Wu *et al.* also studied mixtures of CH<sub>4</sub> and N<sub>2</sub> up to 5.00 bar at 30°C and 50°C and found a slight negative deviation from ideality in the total loading for N<sub>2</sub> compositions greater than 44.9 mol%. Dreisbach *et al.* found that for Norit A1 Extra activated carbon (at 25°C, pressures from 1.08 to 60.35 bar) CH<sub>4</sub> displays a slight positive deviation from ideality in mixtures with N<sub>2</sub> [17]. The average prediction error from the IAS calculations and the experimental loadings was 3.82% with a 5.20% error in the CH<sub>4</sub> loading in particular. Overall, the data for activated carbons in the literature suggests that a CH<sub>4</sub>/N<sub>2</sub> mixture at 30°C and  $\approx 1.00$  bar is either ideal or weakly nonideal.

To test the ability of the  $\mu$ DCB to predict multicomponent adsorption equilibrium, a more challenging system was chosen. Specifically, mixtures of CO<sub>2</sub> and CH<sub>4</sub> on zeolite 13X. The single-component isotherms of CH<sub>4</sub> and CO<sub>2</sub> are shown in Fig. 6d and e. On zeolite 13X, CH<sub>4</sub> exhibits a linear trend in loading and CO<sub>2</sub> is highly nonlinear. Due to the large capacity of CO<sub>2</sub> on zeolite 13X, the adsorptive competition can be expected to be highly non-ideal [7]. Krishna and van Baten predicted non-ideal adsorption of CH<sub>4</sub> in particular (in mixtures with CO<sub>2</sub>) on zeolite 13X at 27°C and 1.00 bar using CBMC simulations [7]. CH<sub>4</sub> adsorption is greater than what is predicted by IAST. Krishna and van Baten also show that the CO<sub>2</sub> loading is virtually unaffected by CH<sub>4</sub> loading. The CH<sub>4</sub>/CO<sub>2</sub> phase-diagram found by Krishna and van Baten is shown in the Supporting Information along ideal and real competitive models. This was also found by Avijegon *et al.*, where the experimental selectivity of CO<sub>2</sub> to CH<sub>4</sub> was  $\approx 3 - 40$  times less than what was predicted by IAST at 0, 30 and 50°C at pressures between 1.06 to 9.03 bar [48].

A series of  $\text{CO}_2/\text{CH}_4$  adsorption experiments were performed on zeolite 13X at  $30^\circ\text{C}$  and  $\approx 1.01$  bar. The mixtures for these experiments were: 5/95, 10/90, 25/50, 50/50 and 75/25 mol%  $\text{CO}_2/\text{CH}_4$  to describe the entire range of competition including a range at low  $\text{CO}_2$  composition where the mixture is expected to deviate significantly from ideality. Desorption was not performed for this set of experiments. For a  $\text{CO}_2$  measurement,  $\text{CH}_4$  was used to saturate the zeolite 13X column at  $30^\circ\text{C}$  and 1.01 bar prior to the adsorption experiment. For a  $\text{CH}_4$  measurement, the zeolite 13X column was initially saturated with  $\text{CO}_2$  at  $30^\circ\text{C}$  and 0.94 bar. These results are shown in Fig. 10b with a sample set of adsorption breakthrough curves for an approximately 50/50 mol%  $\text{CO}_2/\text{CH}_4$  mixture in Fig. 12. Many of the same features as the  $\text{CH}_4/\text{N}_2$  adsorption breakthrough curves are observed in the  $\text{CO}_2/\text{CH}_4$  adsorption experiments. The breakthrough curve of the heavy component,  $\text{CO}_2$ , again resembles a single-component adsorption breakthrough curve. The molar flow in Fig. 12a displays a shock transition and the corresponding effluent flow drops (in Fig. 12c), which returns to  $Q_{\text{in}}$  as  $\text{CO}_2$  breaks through. The methane adsorption breakthrough curve resembles a desorption wave in Fig. 12b and its corresponding effluent flow (in Fig. 12d) increases initially before dropping to  $Q_{\text{in}}$  as  $\text{CO}_2$  desorbs from the column. The corresponding adsorption equilibrium data (hollow markers) is shown in Fig. 10b with IAST predictions as solid lines and equal energy sites (EES) DSL predictions as the dashed line. The EES DSL model is an extended DSL model, where the single-site Langmuir isotherm parameters for the light component are used in a DSL model where the saturation loadings ( $q_b^{\text{sat}}$  and  $q_d^{\text{sat}}$ ) are the same as the heavy component [8]. Note that the EES DSL predictions for  $\text{CO}_2$  are indistinguishable from the IAST predictions. Tabulated equilibrium data is given in Table 7. As seen in Fig. 10b,  $\text{CO}_2$  is unaffected by  $\text{CH}_4$ , as was expected [7]. At almost all  $\text{CO}_2$  compositions, the  $\text{CO}_2$  equilibrium loadings were predicted by IAST and the EES model. Experiments at 10/90 and 25/75 mol%  $\text{CO}_2/\text{CH}_4$  were repeated (when measuring  $\text{CO}_2$ ) to confirm the  $\text{CO}_2$  loadings. All the repeated experiments were the same within the propagated error. The measured  $\text{CH}_4$  equilibrium loadings are highly nonideal. The only two  $\text{CH}_4$  measurements that are

predicted by IAST are at the extremes, either 100 mol% CH<sub>4</sub> or 0 mol% CH<sub>4</sub>. All other measurements, and their associated errors, do not bisect the CH<sub>4</sub> IAST predictions. The measured CH<sub>4</sub>  $\mu$ DCB data all display a positive deviation from IAST, which again was expected [7, 48]. The EES model is able to predict the measured data better than IAST. This trend was also found for the CH<sub>4</sub>/CO<sub>2</sub> CBMC simulations reported by Krishna and van Baten, where the EES model is a very good fit for CH<sub>4</sub> in particular (shown in Supporting Information) [7]. The mixture CO<sub>2</sub>/CH<sub>4</sub> adsorption experiments show that the  $\mu$ DCB is able to determine the binary equilibrium loadings of a highly nonideal system. The CO<sub>2</sub> measurements required thermal activation (at 350°C) between measurements, which made data collection slower. The CO<sub>2</sub> measurements plus thermal activation required about 2 hours each (approximately two work-days), while the CH<sub>4</sub> measurements were completed in a single work-day (8 hours).

## 5 Conclusions

A microscale dynamic column breakthrough ( $\mu$ DCB) apparatus was constructed that is able to quantify gas adsorption and desorption equilibrium loadings of a milligram-scale quantity of adsorbent. Small amounts of adsorbent, 238.9 mg of zeolite 13X and 180.2 mg of activated carbon, were used to perform all breakthrough experiments reported in this study. A typical experiment (at 5 sccm) lasted about 35 minutes and yielded two equilibrium measurements. This allowed for five point binary phase diagrams to be measured in a few work-days (a minimum of 10 – 12 hours). The  $\mu$ DCB was built into an existing GC oven to control temperature and use the onboard thermal conductivity detector for composition measurement. The associated mass balances and description of a blank experiment were provided, and are analogous to a traditional, large-scale DCB system. Single-component adsorption and desorption breakthrough experiments were performed at  $\approx$  0.95 bar and 5.3 sccm with N<sub>2</sub> and CH<sub>4</sub> on zeolite 13X, and activated carbon, at 30, 40 and 50°C. These results agree with statically collected equilibrium data at the same conditions. A series of N<sub>2</sub> adsorption and des-

orption experiments were repeated five times on zeolite 13X and were all found to agree with each other; also, the standard experimental error was less than the propagated error. Methane/nitrogen multicomponent adsorption and desorption experiments were performed on zeolite 13X and activated carbon at  $\approx 0.95$  bar and 5.3 sccm flow. The  $\mu$ DCB measurements for the  $\text{CH}_4/\text{N}_2$  mixtures agreed perfectly with the predictions from ideal adsorbed solution theory. Specifically, the values agreed with the linear isotherm predictions, since typically two linear isotherms do not compete. The light-component adsorption and desorption curves were found to have opposite flow curve than expected. Specifically, the flow curve for a light-component adsorption experiment resembled a desorption experiment and vice versa for desorption. Mixtures of  $\text{CH}_4/\text{N}_2$  on activated carbon were found to be weakly non-ideal depending on the temperature. The adsorption and desorption equilibrium loadings for  $\text{N}_2$  agreed well with IAST, while  $\text{CH}_4$  became more ideal as the temperature increased from  $30^\circ\text{C}$  to  $50^\circ\text{C}$ . The measurements generally agree with the literature, where either  $\text{CH}_4$  was found to be ideal, or weakly nonideal. A highly non-ideal system of  $\text{CO}_2/\text{CH}_4$  was also studied on zeolite 13X at  $30^\circ\text{C}$ . The  $\mu$ DCB measured adsorption loadings showed that  $\text{CO}_2$  was unaffected by  $\text{CH}_4$  adsorption, while  $\text{CH}_4$  displayed a positive deviation from IAST. These results agree with what was found in the literature.

The miniaturization of the DCB system also brings in challenges. For instance, using small quantities of adsorbent may not be representative of the large sample that can be deployed in a process. This can be resolved by performing multiple batches. Further, small amounts of leaks can lead to large errors and presence of strongly adsorbed components, e.g., water can have a major impact on the measurements. Repetition of blank experiments, using reference adsorbents [49], or installing desiccant beds in the gas supply lines [21] can alleviate these challenges. The advantages of the  $\mu$ DCB mainly stem from its ability to be used for very small sample quantities making it ideal for early stage adsorbent development. Although extensive detector calibrations are required, they are not laborious. Thermal conductivity detectors are known to be very stable and reproducible. Once performed, these calibrations hold for a long time. An-

other key feature of the  $\mu$ DCB is the ability to construct it from relatively inexpensive parts. For instance, no proprietary equipment is needed, and the use of the TCD avoids the need of an expensive detector, such as a mass spectrometer. In summary,  $\mu$ DCB can be a valuable addition to the materials scientist with its ability to generate the fast, accurate, and precise measurements both single and binary adsorption equilibrium.

## 6 Acknowledgments

Funding from NSERC and Benchmark International, Edmonton through the NSERC-Alliance program, and Alberta Innovates through the Campus Alberta Small Business Engagement (CASBE), and NSERC Discovery program is acknowledged.

## 7 Declaration of Interests

All authors confirm that there is no conflict of interest to declare.

## 8 Supporting Information

Details of error analysis, pictures of the  $\mu$ DCB system, detailed breakthrough curves of all experiments studied in this work are provided in the Supporting Information.

# Nomenclature

## Roman symbols

$b$	adsorption equilibrium constant [bar <sup>-1</sup> ]
$C$	concentration [mol m <sup>-3</sup> ]
$d$	adsorption equilibrium constant [bar <sup>-1</sup> ]
$D_p/r_p^2$	pore diffusional time constant [s <sup>-1</sup> ]
$f$	function
$H$	Henry Constant [-]
$\Delta H$	heat of adsorption [J mol <sup>-1</sup> ]
$I$	TCD signal [mV]
$K$	Henry constant [mol kg <sup>-1</sup> bar <sup>-1</sup> ]
$L$	ZLC parameter [-]
$m_{\text{ads}}$	adsorbent mass [kg]
$n$	index [-]
$p$	pressure [bar]
$q^*$	equilibrium solid phase loading [mol kg <sup>-1</sup> ]
$r$	radius [m]
$Q$	volumetric flow [m <sup>3</sup> s <sup>-1</sup> ]
$Q(t)$	effluent volumetric flow [m <sup>3</sup> s <sup>-1</sup> ]
$R$	universal gas constant [Pa m <sup>3</sup> mol <sup>-1</sup> K <sup>-1</sup> ]
$t$	time [s]
$\bar{t}$	mean retention time [s]
$T$	temperature [K]
$V$	volume [m <sup>3</sup> ]
$y$	mole fraction [-]
$y(t)$	effluent mole fraction [-]



## Greek symbols

$\delta$	uncertainty
$\gamma$	uncertain variable
$\rho$	density [kg m <sup>-3</sup> ]

## Abbreviations, subscripts and superscripts

ads	adsorption or adsorbent
b	adsorption site
blank	blank response
col	column
comp	composite response or component
d	adsorption site
des	desorption
fluid	fluid accumulation
i	index of species
in	inlet
init	initial
j	index
m	molar
max	maximum
n	index
p	particle
pync	pyncnometric
sat	ultimate saturation
sk	skelletal
std	standard
t	time
0	prefactor

## Acronyms

ADS	adsorption
BPR	back pressure regulator
CBMC	Configurational-bias Monte Carlo
DCB	dynamic column breakthrough
DES	desorption
DSL	dual-site Langmuir
EES	equal-energy sites
GC	gas chromatograph
IAST	ideal adsorbed solution theory
$\mu$ DCB	microscale dynamic column breakthrough
MFC	mass flow controller
MFM	mass flow meter
SSL	single-site Langmuir model
TCD	thermal conductivity detector
VCR	vacuum coupling radiation
ZLC	zero-length column

## References

- [1] D. M. Ruthven. *Principles of Adsorption and Adsorption Processes*. John Wiley & Sons, 1984.
- [2] R. T. Yang. *Gas Separation by Adsorption Processes*. Imperial College Press, 1997.
- [3] S. Sircar. Basic research needs for design of adsorptive gas separation processes. *Ind. Eng. Chem. Res.*, 45(16):5435–5448, 2006.
- [4] A. L. Myers and J. M. Prausnitz. Thermodynamics of mixed-gas adsorption. *AIChE J.*, 11(1):121–127, 1965.
- [5] X. Cai, F. Gharagheizi, L. W. Bingel, D. Shade, K. S. Walton, and D. S. Sholl. A collection of more than 900 gas mixture adsorption experiments in porous materials from literature meta-analysis. *Ind. Eng. Chem. Res.*, 60(1):639–651, 2020.
- [6] M. Hefti, D. Marx, L. Joss, and M. Mazzotti. Adsorption equilibrium of binary mixtures of carbon dioxide and nitrogen on zeolites ZSM-5 and 13X. *Micropor. Mesopor. Mat.*, 215:215–228, 2015.
- [7] R. Krishna and J. M. van Baten. Using molecular simulations for elucidation of thermodynamic nonidealities in adsorption of CO<sub>2</sub>-containing mixtures in NaX zeolite. *ACS Omega*, 5(32):20535–20542, 2020.
- [8] N. S. Wilkins and A. Rajendran. Measurement of competitive CO<sub>2</sub> and N<sub>2</sub> adsorption on zeolite 13X for post-combustion CO<sub>2</sub> capture. *Adsorption*, 25(2):115–133, 2019.
- [9] D. W. Siderius, V. K. Shen, R. D. Johnson III, and R. D. van Zee. NIST/ARPA-E database of novel and emerging adsorbent materials. *National Institute of Standards and Technology, Gaithersburg*, 3, 2018.

- [10] S. Sircar. Recent developments in macroscopic measurement of multicomponent gas adsorption equilibria, kinetics, and heats. *Ind. Eng. Chem. Res.*, 46(10):2917–2927, 2007.
- [11] N. S. Wilkins, J. A. Sawada, and A. Rajendran. Measurement of competitive CO<sub>2</sub> and H<sub>2</sub>O adsorption on zeolite 13X for post-combustion CO<sub>2</sub>. *Adsorption*, 26(5):765–779, 2020.
- [12] N. S. Wilkins, A. Rajendran, and S. Farooq. Dynamic column breakthrough experiments for measurement of adsorption equilibrium and kinetics. *Adsorption*, 27(3):397–422, 2020.
- [13] S. N. Nobar and S. Farooq. Experimental and modeling study of adsorption and diffusion of gases in Cu-BTC. *Chem. Eng. Sci.*, 84:801–813, 2012.
- [14] P. Goyal, M. J. Purdue, and S. Farooq. Adsorption and diffusion of N<sub>2</sub> and CO<sub>2</sub> and their mixture on silica gel. *Ind. Eng. Chem. Res.*, 58(42):19611–19622, 2019.
- [15] Y. Wang and M. D. LeVan. Adsorption equilibrium of binary mixtures of carbon dioxide and water vapor on zeolites 5A and 13X. *J. Chem. Eng. Data*, 55(9):3189–3195, 2010.
- [16] D. Shade, W. P. Mounfield III, Y. Huang, B. Marszalek, and K. S. Walton. An automated multi-component gas adsorption system (MC GAS). *Rev. Sci. Instrum.*, 92(5):054102, 2021.
- [17] F. Dreisbach, R. Staudt, and J. U. Keller. High pressure adsorption data of methane, nitrogen, carbon dioxide and their binary and ternary mixtures on activated carbon. *Adsorption*, 5(3):215–227, 1999.
- [18] S. Ottiger, R. Pini, G. Storti, and M. Mazzotti. Competitive adsorption equilibria of CO<sub>2</sub> and CH<sub>4</sub> on a dry coal. *Adsorption*, 14(4-5):539–556, 2008.

- [19] P. J. E. Harlick and F. H. Tezel. Use of concentration pulse chromatography for determining binary isotherms: comparison with statically determined binary isotherms. *Adsorption*, 9(3):275–286, 2003.
- [20] D. Kennedy and F. H. Tezel. Improved method for determining binary adsorption isotherms by using concentration pulse chromatography: adsorption of CO<sub>2</sub> and N<sub>2</sub> by silicalite at different pressures. *Adsorption*, 20(1):189–199, 2014.
- [21] F. Brandani and D. Ruthven. Measurement of adsorption equilibria by the zero length column (ZLC) technique part 2: binary systems. *Ind. Eng. Chem. Res.*, 42(7):1462–1469, 2003.
- [22] F. Brandani and D. M. Ruthven. The effect of water on the adsorption of CO<sub>2</sub> and C<sub>3</sub>H<sub>8</sub> on type X zeolites. *Ind. Eng. Chem. Res.*, 43(26):8339–8344, 2004.
- [23] D. P. Broom, O. Talu, and M. J. Benham. Integral mass balance (IMB) method for measuring multicomponent gas adsorption equilibria in nanoporous materials. *Ind. Eng. Chem. Res.*, 59(46):20478–20491, 2020.
- [24] S. Ottiger, R. Pini, G. Storti, and M. Mazzotti. Measuring and modeling the competitive adsorption of CO<sub>2</sub>, CH<sub>4</sub>, and N<sub>2</sub> on a dry coal. *Langmuir*, 24(17):9531–9540, 2008.
- [25] S. Brandani and E. Mangano. The zero length column technique to measure adsorption equilibrium and kinetics: lessons learnt from 30 years of experience. *Adsorption*, 27(3):319–351, 2021.
- [26] L. Erden, A. D. Ebner, and J. A. Ritter. Separation of landfill gas CH<sub>4</sub> from N<sub>2</sub> using pressure vacuum swing adsorption cycles with heavy reflux. *Energy Fuels*, 32(3):3488–3498, 2018.
- [27] Y. He, J. H. Yun, and N. A. Seaton. Adsorption equilibrium of binary methane/ethane mixtures in BPL activated carbon: isotherms and calorimetric heats of adsorption. *Langmuir*, 20(16):6668–6678, 2004.

- [28] P. Brea, J. A. Delgado, V. I. Águeda, and M. A. Uguina. Modeling of breakthrough curves of N<sub>2</sub>, CH<sub>4</sub>, CO, CO<sub>2</sub> and a SMR type off-gas mixture on a fixed bed of BPL activated carbon. *Sep. Pur. Tech.*, 179:61–71, 2017.
- [29] B. P. Russell and M. D. Levan. Pore size distribution of BPL activated carbon determined by different methods. *Carbon*, 32(5):845–855, 1994.
- [30] O. Talu, J. Li, R. Kumar, P. M. Mathias, J. D. Moyer Jr., and J. M. Schork. Measurement and analysis of oxygen/nitrogen/5A-zeolite adsorption equilibria for air separation. *Gas Sep. Pur.*, 10(3):149–159, 1996.
- [31] M. Verbraeken, A. Centineo, L. Canobbio, and S. Brandani. Accurate blank corrections for zero length column experiments. *Adsorption*, 27(1):129–145, 2021.
- [32] L. Joss and M. Mazzotti. Modeling the extra-column volume in a small column setup for bulk gas adsorption. *Adsorption*, 18(5-6):381–393, 2012.
- [33] J. M. Miller and A. E. Lawson. Gas chromatographic detector response using carrier gases of low thermal conductivity. *Anal. Chem.*, 37(11):1348–1351, 1965.
- [34] A. J. Rothman and L. A. Bromley. High temperature thermal conductivity of gases. *Ind. Eng. Chem.*, 47(5):899–906, 1955.
- [35] A. L. Lindsay and L. A. Bromley. Thermal conductivity of gas mixtures. *Ind. Eng. Chem.*, 42(8):1508–1511, 1950.
- [36] L. J. Schmauch and R. A. Dinerstein. Response of thermal-conductivity cells in gas chromatography. *Anal. Chem.*, 32(3):343–352, 1960.
- [37] T. Hocker, A. Rajendran, and M. Mazzotti. Measuring and modeling supercritical adsorption in porous solids. carbon dioxide on 13X zeolite and on silica gel. *Langmuir*, 19(4):1254–1267, 2003.

- [38] A. L. Myers and P. A. Monson. Physical adsorption of gases: the case for absolute adsorption as the basis for thermodynamic analysis. *Adsorption*, 20(4):591–622, 2014.
- [39] A. Rajendran, V. Kariwala, and S. Farooq. Correction procedures for extra-column effects in dynamic column breakthrough experiments. *Chem. Eng. Sci.*, 63(10):2696–2706, 2008.
- [40] N. Casas, J. Schell, R. Pini, and M. Mazzotti. Fixed bed adsorption of CO<sub>2</sub>/H<sub>2</sub> mixtures on activated carbon: experiments and modeling. *Adsorption*, 18(2):143–161, 2012.
- [41] N. Casas, J. Schell, R. Blom, and M. Mazzotti. MOF and UiO-67/MCM-41 adsorbents for pre-combustion CO<sub>2</sub> capture by PSA: Breakthrough experiments and process design. *Sep. Pur. Tech.*, 112:34–48, 2013.
- [42] S. A. Peter, G. V. Baron, J. Gascon, F. Kapteijn, and J. F. M. Denayer. Dynamic desorption of CO<sub>2</sub> and CH<sub>4</sub> from amino-MIL-53 (Al) adsorbent. *Adsorption*, 19(6):1235–1244, 2013.
- [43] T. L. H. Saleman, G. C. Y. Watson, T. E. Rufford, P. S. Hofman, K. I. Chan, and E. F. May. Capacity and kinetic measurements of methane and nitrogen adsorption on H<sup>+</sup>-mordenite at 243–303 K and pressures to 900 kPa using a dynamic column breakthrough apparatus. *Adsorption*, 19(6):1165–1180, 2013.
- [44] Y. Park, D. K. Moon, D. Park, M. Mofarahi, and C. H. Lee. Adsorption equilibria and kinetics of CO<sub>2</sub>, CO, and N<sub>2</sub> on carbon molecular sieve. *Sep. Pur. Tech.*, 212:952–964, 2019.
- [45] J. B. Lin, T. T. T. Nguyen, R. Vaidhyanathan, J. Burner, J. M. Taylor, H. Durekova, F. Akhtar, R. K. Mah, O. Ghaffari-Nik, S. Marx, N. Fylstra, S. S. Iremonger, K. W. Dawson, P. Sarkar, P. Hovington, A. Rajendran, T. K. Woo, and

- G. K. H. Shimizu. A scalable metal-organic framework as a durable physisorbent for carbon dioxide capture. *Science*, 374(6574):1464–1469, 2021.
- [46] D. A. Kennedy, M. Mujcin, E. Trudeau, and F. H. Tezel. Pure and binary adsorption equilibria of methane and nitrogen on activated carbons, desiccants, and zeolites at different pressures. *J. Chem. Eng. Data*, 61(9):3163–3176, 2016.
- [47] Y. J. Wu, Y. Yang, X. M. Kong, P. Li, J. G. Yu, A. M. Ribeiro, and A. E. Rodrigues. Adsorption of pure and binary CO<sub>2</sub>, CH<sub>4</sub>, and N<sub>2</sub> gas components on activated carbon beads. *J. Chem. Eng. Data*, 60(9):2684–2693, 2015.
- [48] G. Avijegon, G. Xiao, G. Li, and E. F. May. Binary and ternary adsorption equilibria for CO<sub>2</sub>/CH<sub>4</sub>/N<sub>2</sub> mixtures on zeolite 13X beads from 273 to 333 K and pressures to 900 kPa. *Adsorption*, 24(4):381–392, 2018.
- [49] H. G. T. Nguyen, C. M. Sims, B. Toman, J. Horn, R. D. van Zee, M. Thommes, R. Ahmad, J. F. M. Denayer, G. V. Baron, E. Napolitano, M. Bielewski, E. Mangano, S. Brandani, D. P. Broom, M. J. Benham, A. Dailly, F. Dreisbach, S. Edubilli, S. Gumma, J. Möllmer, M. Lange, M. Tian, T. J. Mays, T. Shigeoka, S. Yamakita, M. Hakuman, Y. Nakada, K. Nakai, J. Hwang, R. Pini, H. Jiang, A. D. Ebner, M. A. Nicholson, J. A. Ritter, J. Farrando-Pérez, C. Cuadrado-Collados, J. Silvestre-Albero, C. Tampaxis, T. Steriotis, D. Řimnáčová, M. Švábová, M. Vorokhta, H. Wang, E. Bovens, N. Heymans, and G. De Weireld. A reference high-pressure CO<sub>2</sub> adsorption isotherm for ammonium ZSM-5 zeolite: results of an interlaboratory study. *Adsorption*, 24(6):531–539, 2018.



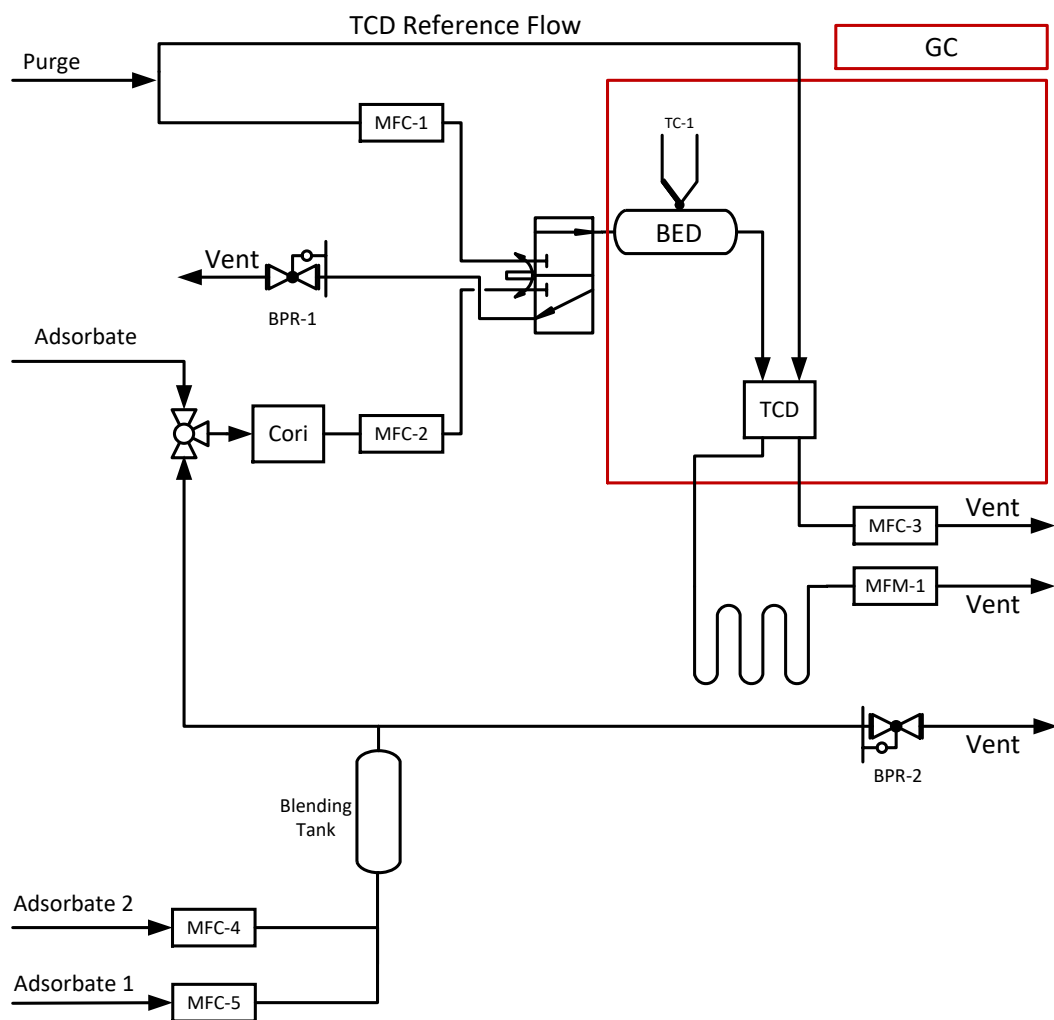


Figure 1: General arrangement of components and instrumentation for the  $\mu$ DCB system.

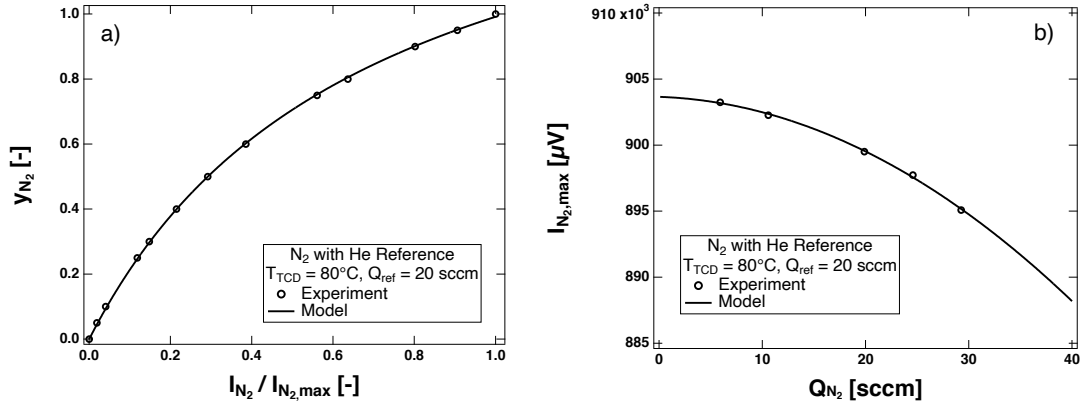


Figure 2: N<sub>2</sub>/He thermal conductivity detector calibrations at a TCD block temperature of 80°C and a He reference flowrate of 20 sccm. Panel (a) shows the mole fraction of N<sub>2</sub> as a function of the normalized TCD signal. Panel (b) shows the effect of analyzing gas flow on the 100% N<sub>2</sub> TCD signal; this maximum signal is used to normalize the TCD signal in panel (a). The markers denote experimentally collected data and the lines are empirical fits.

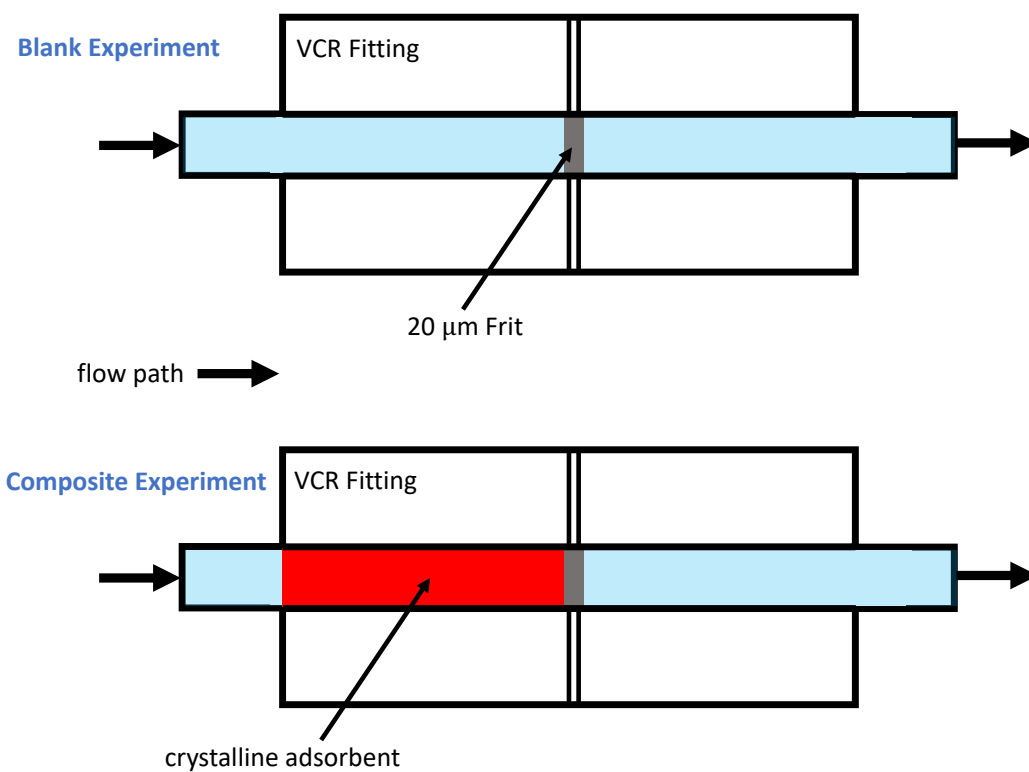


Figure 3: Schematic of the blank and composite fluid volumes in the  $\mu$ DCB apparatus. The blank volume, shown as the blue shaded area, contains all upstream, column, and downstream volumes. The composite experiment contains less fluid volume due to the volume occupied by the adsorbent (shown in red).

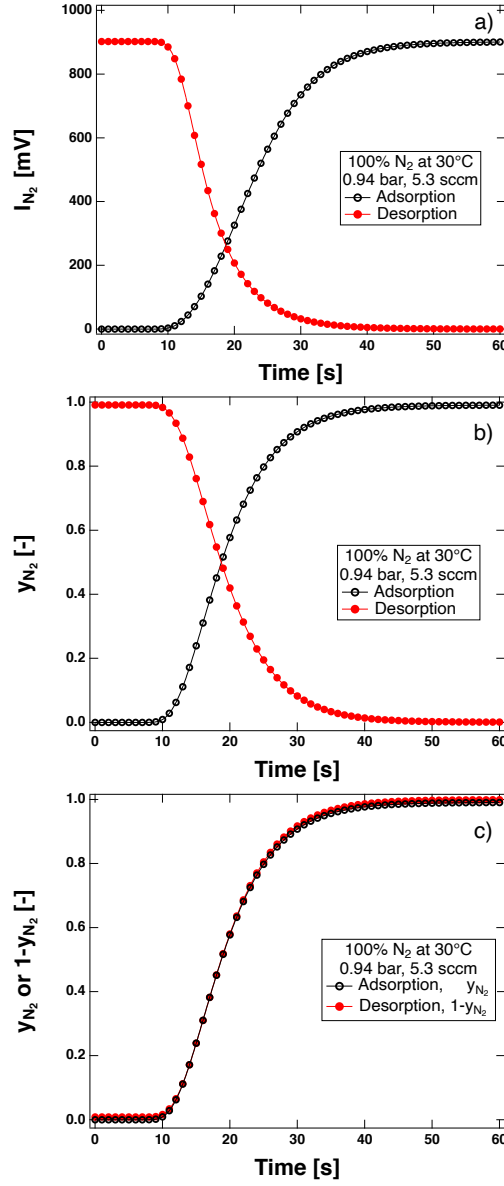


Figure 4: Single-component  $N_2/He$  adsorption and desorption blank responses at 0.94 bar and 30°C. Panel (a) shows the unprocessed TCD signal in mV. Panel (b) shows the adsorption and desorption curves as is and (c) transforms the desorption curve by  $1 - y_{N_2}$  to be directly comparable to the adsorption blank. Note that in panel (c), the adsorption and desorption experiments overlap. The adsorption curves are shown with hollow symbols and desorption curves are shown with the solid symbols. The reference gas was He for these experiments.

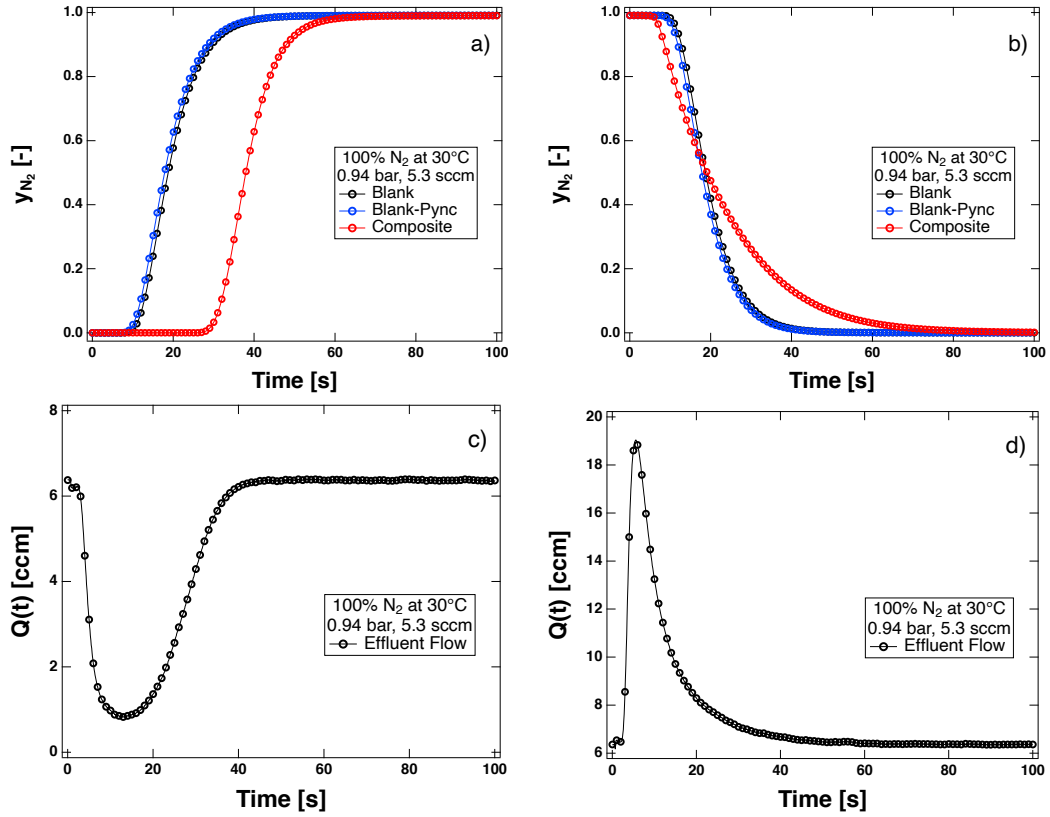


Figure 5: Single-component  $N_2/He$  adsorption and desorption  $\mu$ DCB experiment for 100 mol%  $N_2$  in He on zeolite 13X at 0.94 bar and 30°C. The top row shows the (a) adsorption and (b) desorption curves. The corresponding effluent flow curves for (c) adsorption and (d) desorption are shown below the mole fraction responses. The reference gas was He for these experiments.

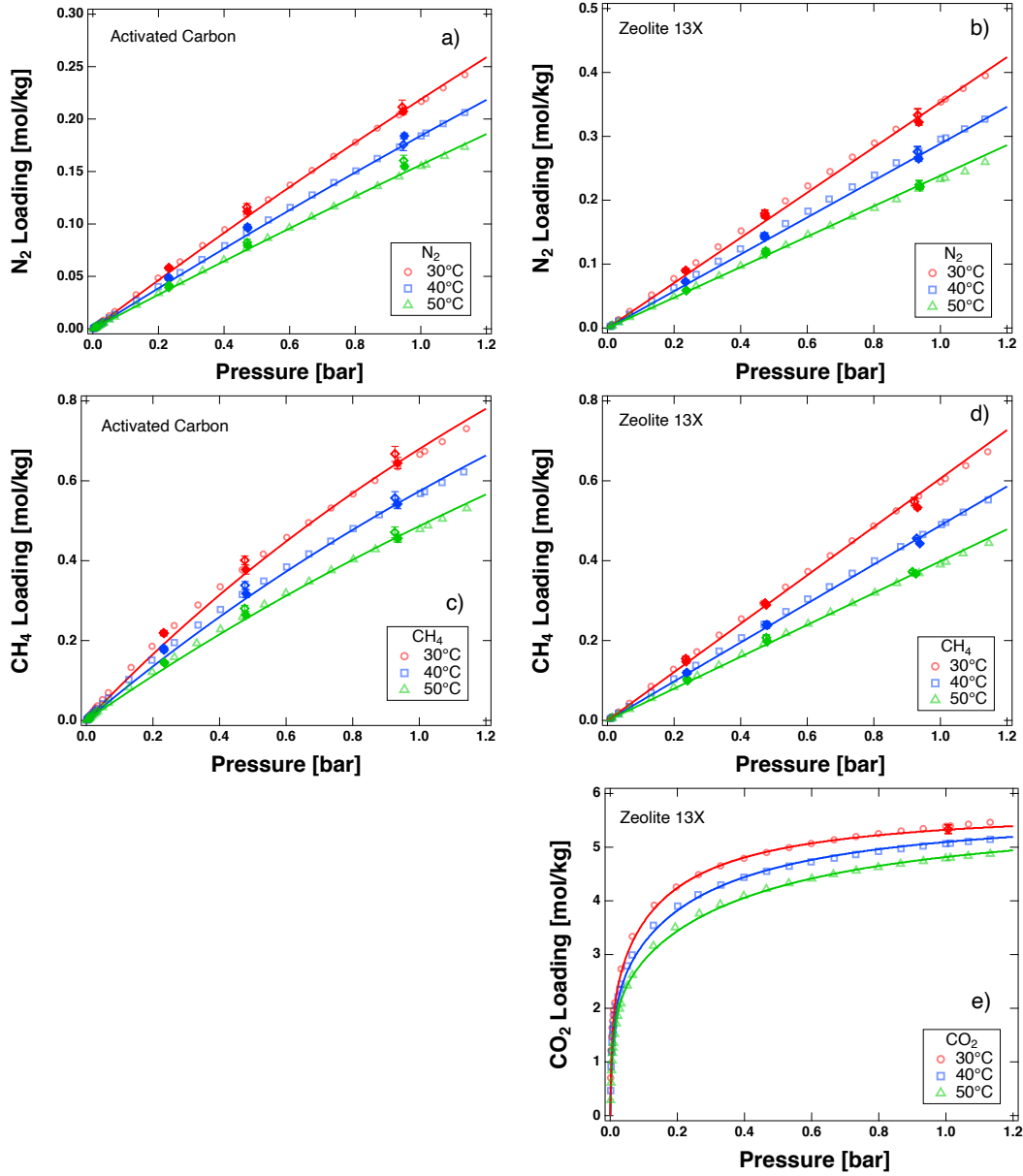


Figure 6: Single-component equilibrium data of  $N_2$  (a, b) and  $CH_4$  (c, d) on activated carbon and zeolite 13X at 30, 40 and 50°C. Panel (e) contains single-component equilibrium data for  $CO_2$  at 30, 40 and 50°C on zeolite 13X. Hollow diamond markers are adsorption breakthrough experiments, and solid diamond markers are desorption experiments. Circle, square and triangle markers are volumetrically collected equilibrium data. Linear, single-site or dual-site Langmuir isotherms are shown with lines.

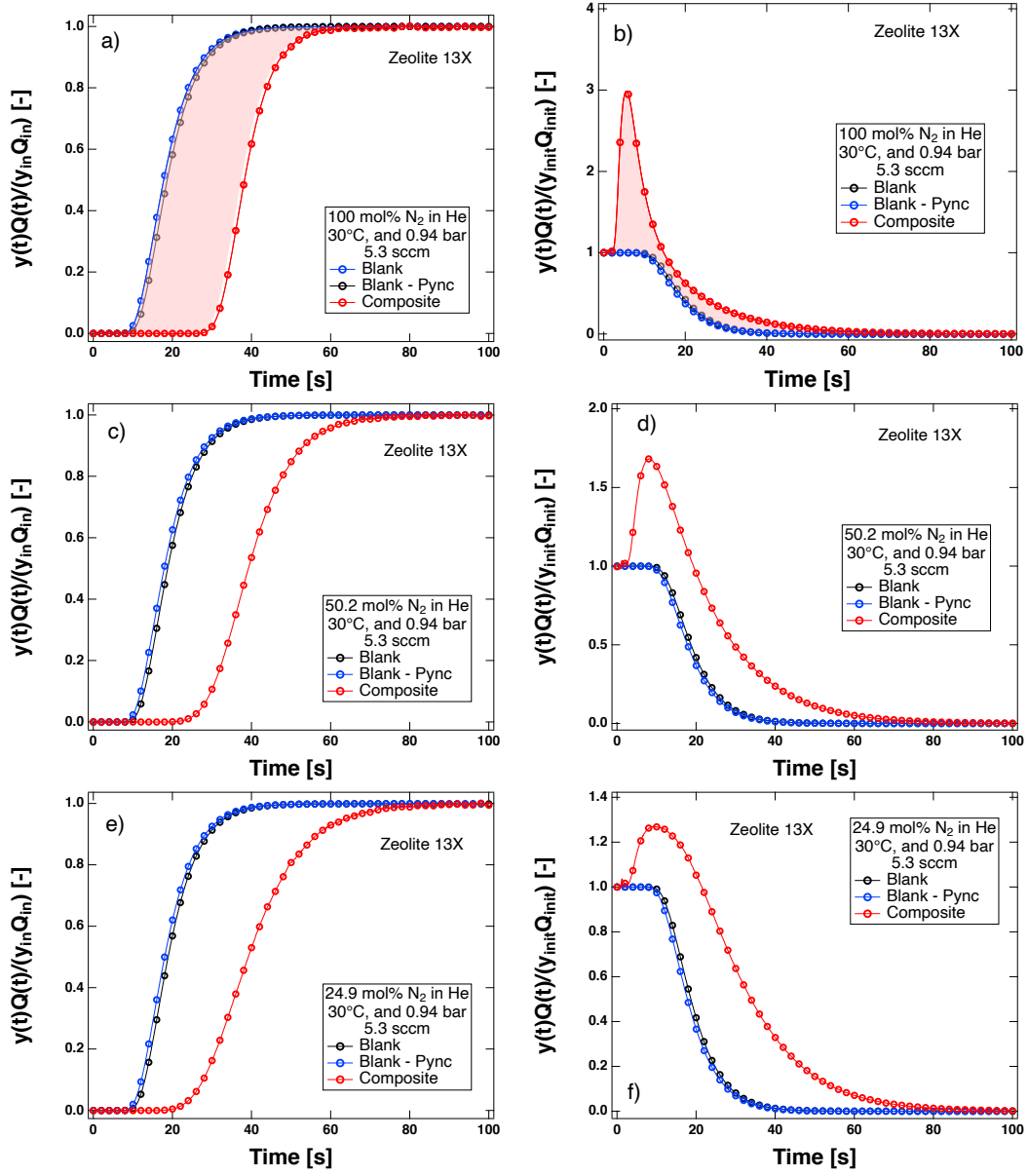


Figure 7: Single-component  $N_2/He$  adsorption (left) and desorption (right) breakthrough curves at 0.94 bar and 30°C on zeolite 13X. Panels (a) and (b) are for 100 mol%  $N_2$ , (c) and (d) are for 50.2 mol%  $N_2/He$ , and (e) and (f) are for 24.9 mol%  $N_2/He$ . The reference gas was He for these experiments. Every tenth point is shown as a marker.

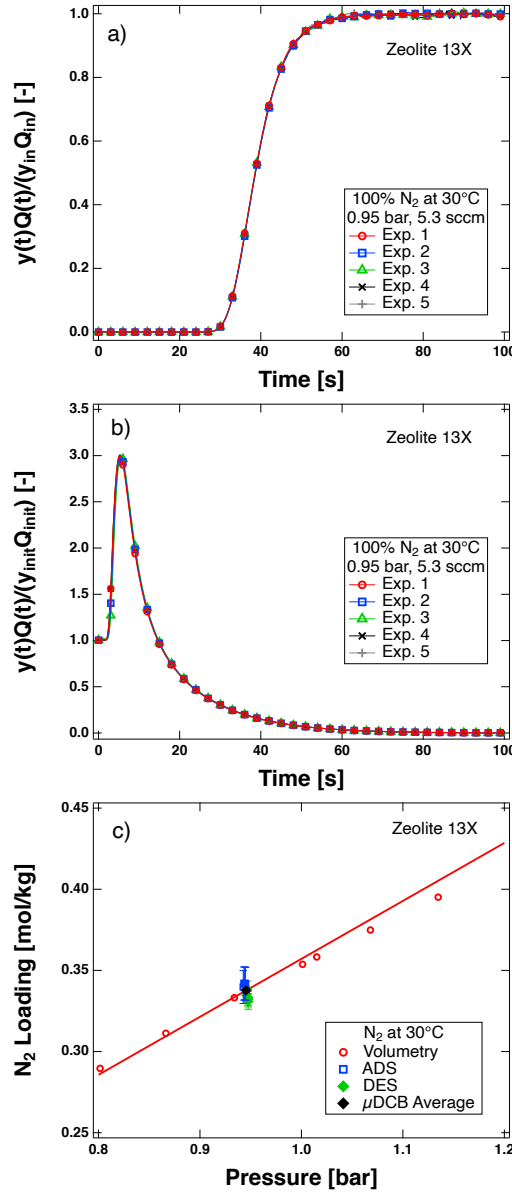


Figure 8: A series of single-component  $N_2$ /He adsorption and desorption  $\mu$ DCB experiments for 100 mol%  $N_2$  in He on zeolite 13X at  $\approx 0.95$  bar and  $30^\circ\text{C}$ . The (a) adsorption and (b) desorption normalized molar flow curves. Every thirtieth point is shown as a marker. (c) The corresponding equilibrium loadings of  $N_2$  for the five adsorption and desorption experiments with the isotherm and volumetrically collected data. The reference gas was He for these experiments.



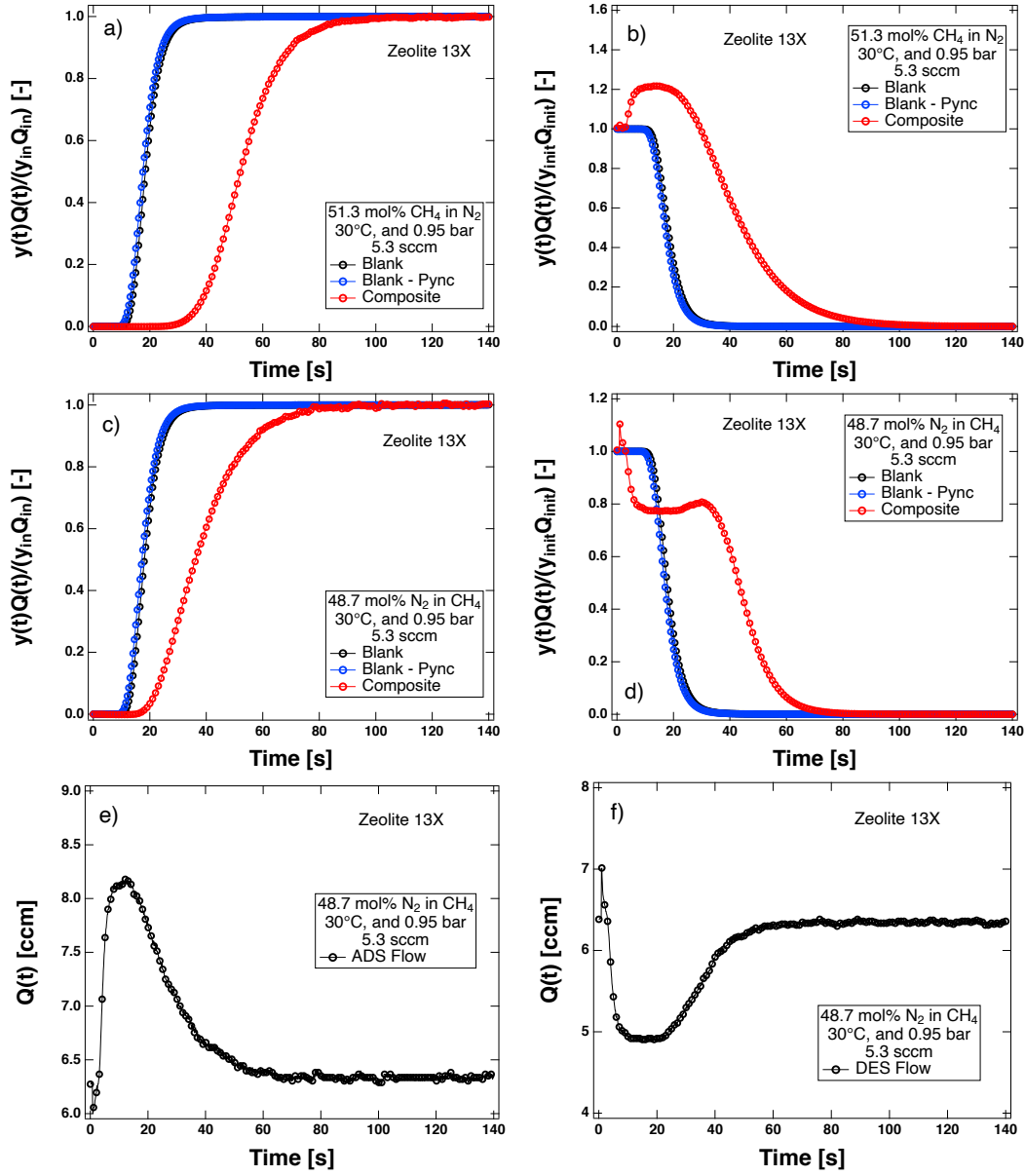


Figure 9: Multicomponent adsorption (left) and desorption (right) breakthrough curves on zeolite 13X at 0.95 bar and 30°C for a 51.3/48.7 mol% CH<sub>4</sub>/N<sub>2</sub> mixture. Panels (a) and (b) are adsorption and desorption of CH<sub>4</sub>, and panels (c) and (d) are equivalent experiments for N<sub>2</sub>. Panels (e) and (f) show the corresponding effluent flow curves for the N<sub>2</sub> experiments. Every tenth point is shown as a marker. Note that the CH<sub>4</sub> and N<sub>2</sub> experiments are separate experiments, since the TCD reference changes to detect one gas over the other. The reference gas was N<sub>2</sub> for the CH<sub>4</sub> experiment and CH<sub>4</sub> for the N<sub>2</sub> experiment.

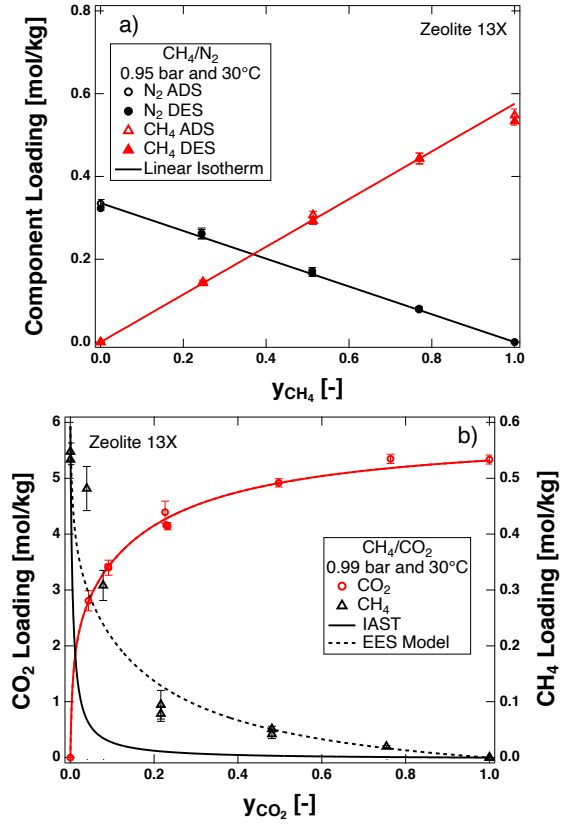


Figure 10: Multi-component equilibrium data of (a) CH<sub>4</sub>/N<sub>2</sub> mixtures and (b) CO<sub>2</sub>/CH<sub>4</sub> on zeolite 13X at 30°C. Hollow markers are adsorption breakthrough experiments, and solid markers are desorption experiments. Solid lines are ideal adsorbed solution theory predictions and dashed lines are equal-energy sites predictions.

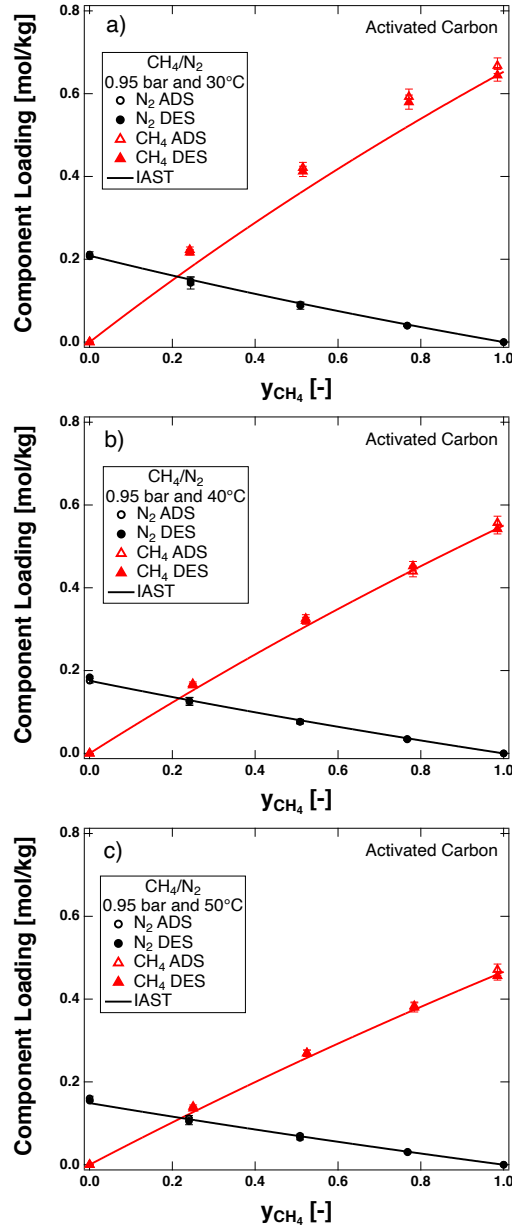


Figure 11: Multi-component equilibrium data of  $\text{CH}_4/\text{N}_2$  mixtures on activated carbon at (a) 30°C, (b) 40°C and (c) 50°C and 0.95 bar. Hollow markers are adsorption breakthrough experiments, and solid markers are desorption experiments. Solid lines are ideal adsorbed solution theory predictions.

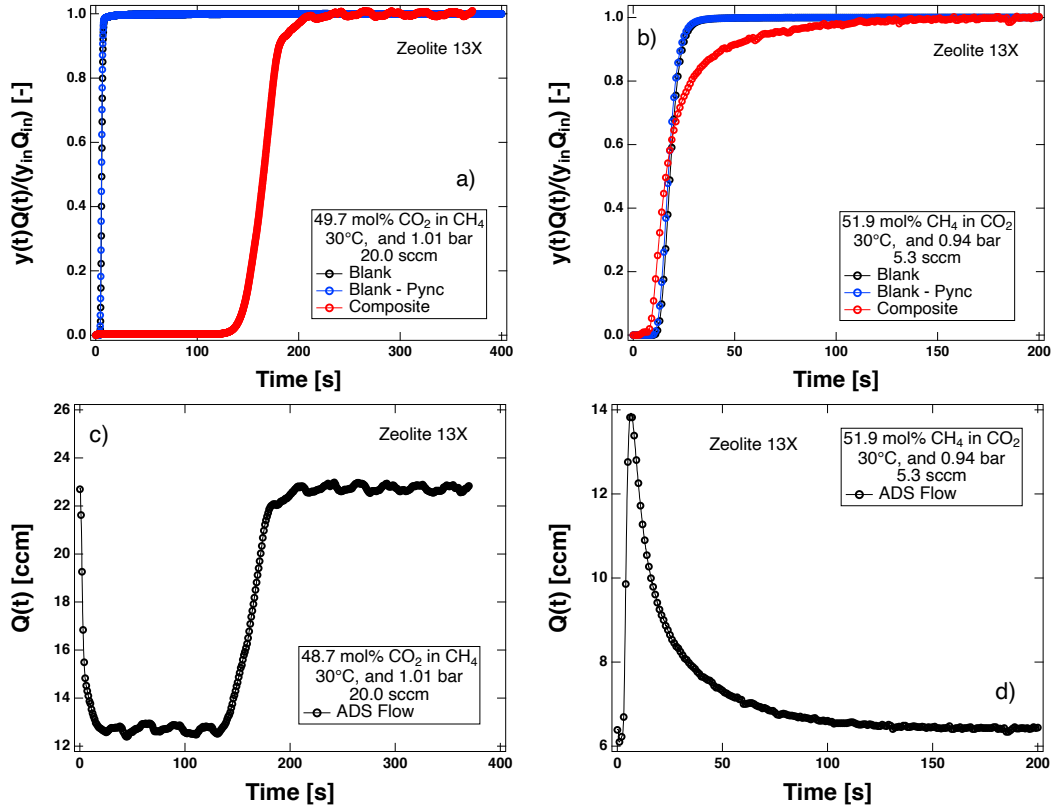


Figure 12: Two multicomponent CO<sub>2</sub>/CH<sub>4</sub> adsorption breakthrough experiments on zeolite 13X at 30°C. Panel (a) shows the adsorption breakthrough of 49.7 mol% CO<sub>2</sub> in CH<sub>4</sub> at 1.01 bar and 20.0 sccm inlet flow. Panel (b) shows the adsorption breakthrough of 51.9 mol% CH<sub>4</sub> in CO<sub>2</sub> at 0.94 bar and 5.3 sccm inlet flow. Two separate experiments were required to find both CO<sub>2</sub> and CH<sub>4</sub> loadings. Panels (c) and (d) show the corresponding effluent flow curves for the multicomponent CO<sub>2</sub>/CH<sub>4</sub> experiments. The reference gas was CH<sub>4</sub> for the CO<sub>2</sub> experiment and CO<sub>2</sub> for the CH<sub>4</sub> experiment. Every tenth point is shown as a marker.

Table 1: Measured variables and their associated uncertainties for the calculation of equilibrium loading with the micro dynamic column breakthrough mass balance.

Measured Variable		Uncertainty
$m_{\text{ads}}$		0.0005 g
$P$		$3.45 \times 10^{-4}$ bar
$T$		1 K
$\rho_{\text{sk}}$		0.2 g/mL
$y_{\text{in}}$	1 mV ( $\approx 0.001$ to 0.04, depends on gas mixture)	
$y(t)$	1 mV ( $\approx 0.001$ to 0.04, depends on gas mixture)	
$Q_{\text{in}}$		0.02 g/h
$Q(t)$		$(0.006)Q_{\text{in}}$ ccm

Table 2: Isotherm parameters for single component N<sub>2</sub>, CH<sub>4</sub> and CO<sub>2</sub> equilibrium on activated carbon and zeolite 13X.

Material	Gas	Model	$q_b^{\text{sat}}$ [mol kg <sup>-1</sup> ]	$q_d^{\text{sat}}$ [mol kg <sup>-1</sup> ]	$b_0$ [bar <sup>-1</sup> ]	$d_0$ [bar <sup>-1</sup> ]	$K_0$ [mol bar <sup>-1</sup> kg <sup>-1</sup> ]	$-\Delta H_b$ [kJ mol <sup>-1</sup> ]	$-\Delta H_d$ [kJ mol <sup>-1</sup> ]
Zeolite 13X	CO <sub>2</sub>	DSL	2.375	3.421	$1.675 \times 10^{-2}$	$2.400 \times 10^{-6}$	-	23.80	37.30
Zeolite 13X	CH <sub>4</sub>	DSL	2.375	3.421	$7.660 \times 10^{-5}$	$7.660 \times 10^{-5}$	-	18.44	18.44
Zeolite 13X	CH <sub>4</sub>	Linear	-	-	-	-	$7.024 \times 10^{-4}$	17.04	-
Zeolite 13X	N <sub>2</sub>	Linear	-	-	-	-	$6.185 \times 10^{-4}$	16.00	-
Activated Carbon	CH <sub>4</sub>	SSL	3.016	-	$3.657 \times 10^{-4}$	-	-	16.83	-
Activated Carbon	N <sub>2</sub>	SSL	3.016	-	$2.391 \times 10^{-4}$	-	-	14.59	-

Table 3: Conditions for the zeolite 13X  $\mu$ DCB single-component adsorption and desorption experiments performed in this study.

Gas	$y_{\text{in/init}}$ [-]	$P$ [bar]	$T$ [°C]	$Q_{\text{in}}$ [ccm]	$q_{\text{ads}}^*$ [mol kg <sup>-1</sup> ]	$q_{\text{des}}^*$ [mol kg <sup>-1</sup> ]
N <sub>2</sub> /He	1.000	0.943	30	6.36	0.3346	0.3229
	0.502	0.945	30	6.35	0.1795	0.1755
	0.249	0.944	30	6.36	0.0904	0.0895
	1.000	0.943	40	6.57	0.2759	0.2650
	0.502	0.941	40	6.57	0.1445	0.1419
	0.249	0.942	40	6.57	0.0727	0.0724
	1.000	0.947	50	6.73	0.2242	0.2209
	0.502	0.947	50	6.73	0.1205	0.1171
	0.250	0.948	50	6.72	0.0590	0.0587
CH <sub>4</sub> /He	1.000	0.945	30	6.38	0.5478	0.5335
	0.504	0.945	30	6.36	0.2940	0.2893
	0.249	0.947	30	6.34	0.1547	0.1473
	1.000	0.955	40	6.51	0.4561	0.4432
	0.503	0.955	40	6.49	0.2393	0.2391
	0.250	0.958	40	6.48	0.1198	0.1189
	1.000	0.945	50	6.77	0.3726	0.3674
	0.503	0.954	50	6.70	0.2071	0.1980
	0.252	0.954	50	6.69	0.1039	0.0996

Table 4: Conditions for the activated carbon  $\mu$ DCB single-component adsorption and desorption experiments performed in this study.

Gas	$y_{\text{in/init}}$ [-]	$P$ [bar]	$T$ [°C]	$Q_{\text{in}}$ [ccm]	$q_{\text{ads}}^*$ [mol kg <sup>-1</sup> ]	$q_{\text{des}}^*$ [mol kg <sup>-1</sup> ]
N <sub>2</sub> /He	1.000	0.954	30	6.29	0.2115	0.2073
	0.494	0.953	30	6.29	0.1161	0.1121
	0.243	0.954	30	6.29	0.0579	0.0586
	1.000	0.958	40	6.46	0.1758	0.1840
	0.495	0.954	40	6.49	0.0972	0.0961
	0.243	0.954	40	6.49	0.0491	0.0476
	1.000	0.958	50	6.66	0.1604	0.1549
	0.494	0.954	50	6.68	0.0824	0.0796
	0.243	0.954	50	6.69	0.0395	0.0415
CH <sub>4</sub> /He	1.000	0.949	30	6.34	0.6676	0.6446
	0.500	0.958	30	6.27	0.4013	0.3777
	0.242	0.963	30	6.24	0.2194	0.2182
	1.000	0.949	40	6.54	0.5571	0.5421
	0.500	0.958	40	6.47	0.3384	0.3184
	0.242	0.963	40	6.44	0.1813	0.1765
	1.000	0.950	50	6.74	0.4712	0.4561
	0.500	0.957	50	6.68	0.2804	0.2649
	0.243	0.964	50	6.63	0.1453	0.1441



Table 5: Conditions for the multicomponent CH<sub>4</sub>/N<sub>2</sub>  $\mu$ DCB adsorption and desorption breakthrough performed on zeolite 13X.

$y_{\text{CH}_4}$	$y_{\text{N}_2}$	$P$	$T$	$Q_{\text{in}}$	$q_{\text{N}_2,\text{ads}}^*$	$q_{\text{N}_2,\text{des}}^*$	$q_{\text{CH}_4,\text{ads}}^*$	$q_{\text{CH}_4,\text{des}}^*$
[-]	[-]	[bar]	[°C]	[ccm]	[mol kg <sup>-1</sup> ]	[mol kg <sup>-1</sup> ]	[mol kg <sup>-1</sup> ]	[mol kg <sup>-1</sup> ]
0.247	0.753	0.951	30	6.31	-	-	0.1456	0.1426
0.244	0.756	0.945	30	6.34	0.2630	0.2606	-	-
0.513	0.487	0.950	30	6.32	-	-	0.3072	0.2928
0.511	0.489	0.945	30	6.33	0.1720	0.1663	-	-
0.770	0.230	0.950	30	6.32	-	-	0.4441	0.4432
0.769	0.231	0.945	30	6.34	0.0811	0.0784	-	-

Table 6: Conditions for the multicomponent CH<sub>4</sub>/N<sub>2</sub>  $\mu$ DCB adsorption and desorption experiments performed on activated carbon.

$y_{\text{CH}_4}$	$y_{\text{N}_2}$	$P$	$T$	$Q_{\text{in}}$	$q_{\text{N}_2,\text{ads}}^*$	$q_{\text{N}_2,\text{des}}^*$	$q_{\text{CH}_4,\text{ads}}^*$	$q_{\text{CH}_4,\text{des}}^*$
[-]	[-]	[bar]	[°C]	[ccm]	[mol kg <sup>-1</sup> ]	[mol kg <sup>-1</sup> ]	[mol kg <sup>-1</sup> ]	[mol kg <sup>-1</sup> ]
0.242	0.758	0.958	30	6.28	-	-	0.2227	0.2167
0.243	0.757	0.944	30	6.36	-	-	0.2214	0.2166
0.244	0.756	0.930	30	6.43	0.1476	0.1428	-	-
0.515	0.485	0.947	30	6.34	-	-	0.4210	0.4126
0.515	0.485	0.944	30	6.36	-	-	0.4239	0.4095
0.509	0.491	0.929	30	6.44	0.0910	0.0879	-	-
0.771	0.229	0.945	30	6.36	-	-	0.5927	0.5798
0.767	0.233	0.926	30	6.48	0.0399	0.0396	-	-
0.249	0.751	0.953	40	6.50	-	-	0.1679	0.1646
0.241	0.759	0.954	40	6.47	0.1272	0.1257	-	-
0.522	0.478	0.952	40	6.51	-	-	0.3255	0.3204
0.508	0.492	0.952	40	6.48	0.0763	0.0766	-	-
0.781	0.219	0.953	40	6.51	-	-	0.4395	0.4523
0.767	0.233	0.953	40	6.49	0.0349	0.0338	-	-
0.250	0.750	0.950	50	6.71	-	-	0.1404	0.1360
0.240	0.760	0.951	50	6.69	0.1123	0.1050	-	-
0.525	0.475	0.954	50	6.69	-	-	0.2694	0.2696
0.508	0.492	0.950	50	6.70	0.0701	0.0649	-	-
0.784	0.216	0.954	50	6.70	-	-	0.3799	0.3836
0.768	0.232	0.950	50	6.71	0.0312	0.0300	-	-

Table 7: Conditions for the multicomponent CO<sub>2</sub>/CH<sub>4</sub>  $\mu$ DCB adsorption experiments performed on zeolite 13X.

$y_{\text{CO}_4}$	$y_{\text{CH}_4}$	$P$	$T$	$Q_{\text{in}}$	$q_{\text{CH}_4,\text{ads}}^*$	$q_{\text{CO}_2,\text{ads}}^*$
[-]	[-]	[bar]	[°C]	[ccm]	[mol kg <sup>-1</sup> ]	[mol kg <sup>-1</sup> ]
0.043	0.957	1.01	30	22.88	-	2.8078
0.039	0.961	0.948	30	6.36	0.4816	-
0.090	0.910	1.01	30	22.88	-	3.4193
0.091	0.909	1.01	30	22.88	-	3.3997
0.078	0.922	0.936	30	6.42	0.3082	-
0.226	0.774	0.941	30	6.37	-	4.3939
0.232	0.768	1.01	30	22.72	-	4.1415
0.216	0.784	0.936	30	6.44	0.0785	-
0.497	0.503	1.01	30	22.74	-	4.9188
0.481	0.519	0.938	30	6.41	0.0512	-
0.764	0.236	1.01	30	22.36	-	5.3485
0.754	0.246	0.946	30	6.34	0.0197	-
1.000	0.000	1.01	30	22.36	-	5.3367